Università degli Studi di Cagliari

DOTTORATO DI RICERCA

FISICA DELLA MATERIA

Ciclo XXV

TITOLO TESI

LOW DIMENSION POLYMER-BASED NANOSTRUCTURES FOR PHOTOVOLTAICS

Settore/i scientifico disciplinari di afferenza

FIS 03 / FISICA DELLA MATERIA

Presentata da:	CLAUDIA CADDEO
Coordinatore Dottorato	Prof. PAOLO RUGGERONE
Tutor/Relatore	Prof. LUCIANO COLOMBO Dott. ALESSANDRO MATTONI

Esame finale anno accademico 2011 – 2012

LOW DIMENSION POLYMER-BASED NANOSTRUCTURES FOR PHOTOVOLTAICS

Theoretical investigation on morphology and optoelectronic properties of P3HT-ZnO and P3HT-SWNT nanosystems

CLAUDIA CADDEO

Università degli Studi di Cagliari
Facoltà di Scienze
Dipartimento di Fisica

Relatori:
Prof. Luciano Colombo
Dott. Alessandro Mattoni

ABSTRACT

In this thesis it is discussed the effect of the low dimensionality on several physical properties of hybrid nanostructures for new generation photovoltaics. We investigated several hybrid and organic model systems, consisting of an organic polymer playing the role of electron donor and a low-dimension nanostructure (1D or 0D) which acts as electron acceptor and transporter. Model potential molecular dynamics has been used to characterize the polymer morphology onto the nanostructured substrates. In particular, the wrapping phenomena on one-dimensional structures (ZnO nanoneedles and carbon nanotubes) have been analyzed as a function of several physical variables such as temperature, substrate crystallography, polymer chain length and density. It has been thus possible to observe that wrapped configurations are only metastable on carbon nanotubes at room temperature and in absence of solvents. Nevertheless, wrapped configurations induced by the solvent can be frozen due to the interactions among neighboring polymer chains. According to this study, it is possible to enhance the polymer-nanotube alignment (and thus improving the polymer transport properties) through a suitable tuning of the synthesis parameters. Conversely, wrapped geometries are stable on ZnO nanoneedles, due to the small polymer mobility on the ZnO surface. The results obtained on the morphology of polymer-ZnO hybrids have then been used as a starting point to evaluate the electronic structure and the optical absorption properties. Hybrid models consisting in a 120-atoms ZnO nanoparticle and a set of oligothiophenes have been studied through the density functional theory, and the energy-level alignment has been obtained by using the Δ-self-consistent-field method. 120-atoms ZnO nanoparticles have been synthesized and found to be particularly stable. They therefore not only represent a useful model for computational studies, but are also of potential technological interest. An important result thus obtained is to demonstrate that the interaction between the two organic/inorganic moieties shifts the energy levels, giving rise to a non-staggered junction. This phenomenon is not present in planar ZnO substrates, but it is rather induced by the nanostructuration of the hybrid polymer/metal oxide system. From

the methodological standpoint, a simplified model to predict the energy-level alignment at the interface has been developed, allowing to spare computational resources. Finally, since the atomic configuration of the 120-atoms ZnO nanoparticles is unknown, we calculated the optical absorption spectra in the near ultra-violet of a set of $Zn_{60}O_{60}$ isomers: this information can be compared to experimental spectroscopic data and can thus be used to elucidate the most abundant structure of this cluster.

The results of the present work suggest that the use of nanostructures, although opening interesting technological possibilities such as increasing the donor/acceptor interface, also requires a critical readdressing of our understanding of morphologies and electronic level alignment in low-dimension systems.

SOMMARIO

In questa tesi si discute l'effetto della bassa dimensionalità su diverse proprietà fisiche delle nanostrutture ibride utilizzate per il fotovoltaico di nuova generazione. Sono stati studiati diversi sitemi modello ibridi ed organici, costituiti da un polimero organico che svolge il ruolo di donore di elettroni e da una nanostruttura a bassa dimensionalità (1D o 0D) che ha il compito di raccogliere e trasportare gli elettroni. La dinamica molecolare da potenziali modello è stata utilizzata per caratterizzare la morfologia del polimero all'interfaccia con il substrato nanostrutturato. In particolare, i fenomeni di arrotolamento su strutture monodimensionali (nanofili di ZnO e nanotubi di carbonio) sono stati analizzati in relazione a diverse variabili fisiche, quali temperatura, cristallografia dei substrati, lunghezza e densità delle catene polimeriche. È stato così possibile determinare che le configurazioni arrotolate sono metastabili sui nanotubi di carbonio a temperatura ambiente ed in assenza del solvente. Ciò nonostante, le configurazoni arrotolate indotte dal solvente durante il processo di sintesi possono essere congelate a causa delle interazioni tra catene vicine. Secondo questo studio è dunque in principio possibile migliorare l'allineamento tra le catene polimeriche ed i nanotubi (e di conseguenza le proprietà di trasporto del polimero) tramite una opportuna selezione dei parametri di sintesi. Quando il materiale accettore è costituito da un nanofilo di ZnO, invece, le geometrie arrotolate sono stabili a causa della bassa mobilità

del polimero sullo ZnO. Le indicazioni ottenute sulla morfologia degli ibridi polimero-ZnO sono poi state utilizzate come punto di partenza per determinare la struttura elettronica e le proprietà di assorbimento ottico. Modelli di ibrido costituiti da una nanoparticella da 120 atomi di ZnO e diversi oligotiofeni sono stati studiati tramite la teoria del funzionale densità e l'allineamento dei livelli energetici è stato determinato tramite il metodo Δ-self-consistent-field. Nanoparticelle di ZnO da 120 atomi sono state realizzate e sono particolarmente stabili, e dunque non rappresentano solo un modello utile a fini computazionali, ma sono effettivamente di potenziale interesse tecnologico ed applicativo. Un importante risultato qui ottenuto è mostrare che l'interazione tra i due componenti organico/inorganico dà luogo ad una traslazione dei livelli energetici che porta ad un allineamento non di tipo II (staggered). Questo fenomeno non è presente su substrati planari di ZnO, ma è piuttosto un effetto indotto dalla nanostrutturazione del sistema ibrido polimero/metalossido. Dal punto di vista metodologico, è stato anche sviluppato un modello semplificato per la predizione dell'allineamento dei livelli che permette di risparmiare risorse computazionali. Infine, poichè non si conosce la struttura atomica delle nanoparticelle di ZnO da 120 atomi, sono stati calcolati gli spettri di assorbimento ottico di una serie di isomeri di queste ultime: questo tipo di informazione è confrontabile con eventuali dati spettroscopici sperimentali, e potrà quindi essere utilizzata per determinare la struttura più abbondante dello $Zn_{60}O_{60}$.

I risultati della presente tesi suggeriscono che l'uso di nanostrutture ibride, sebbene apra interessanti possibilità tecnologiche come l'aumento dell'interfaccia donore/accettore, richiede di rivedere criticamente la nostra comprensione della morfologia e dell'allineamento dei livelli elettronici in sistemi a bassa dimensionalità.

PUBLICATIONS

The results of this thesis have been published as follows:

[1] **C. Caddeo**, C. Melis, L. Colombo, A. Mattoni, Understanding the Helical Wrapping of P3HT on Carbon Nanotubes, *J. Phys. Chem. C* **114**, 21109-21113 (2010)

[2] **C. Caddeo**, R. Dessì, C. Melis, L. Colombo, A. Mattoni, Poly(3-hexylthiophene) Adhesion on Zinc Oxide Nanoneedles, *J. Phys. Chem. C* **115**, 16833-16837 (2011)

[3] **C. Caddeo**, G. Malloci, G.M. Rignanese, L. Colombo, A. Mattoni, Electronic properties of hybrid zinc oxide-oligothiophenes nanostructures, *J. Phys. Chem. C* **116**, 8174-8180 (2012)

[4] **C. Caddeo**, G. Malloci, F. De Angelis, L. Colombo, A. Mattoni, Optoelectronic properties of $(ZnO)_{60}$ isomers, *PCCP* **14**, 14293-14298 (2012)

corporibus caecis igitur natura gerit res

— Lucrezio

ACKNOWLEDGMENTS

First of all I would like to thank my supervisors Luciano Colombo and Alessandro Mattoni for their continuous support and motivation. My PhD experience would not have been as pleasant as it has been without their supervison, patience and help. My gratitude also goes to Claudio Melis and Giuliano Malloci for having invested a great amount of their time in helping and teaching me many things on computational physics in the first (and not only) stages of my PhD. I would also like to thank Gian-Marco Rignanese, Filippo De Angelis and Fabio Della Sala for fruitful collaboration, and Matteo Dessalvi for his fundamental technical support.

I am also thankful to my lunchmates Attilio, Paolo, Matteo, Giuseppe, Eric, Shail, Lori, Giorgia and everyone else who shared table & lunch with me in the common room.

Inoltre vorrei ringraziare tutte le persone che hanno contribuito alla mia serenità personale durante questi tre anni di tesi. Innanzitutto la mia famiglia, che mi è sempre stata vicina e alla quale devo praticamente tutto. I miei amici a Cagliari, Iglesias e nel resto del mondo, per la loro allegria ma anche per i discorsi seri, per le grigliate in terrazza, l'irse de tapas, il Reina Sofia e il wino grzane.

Last but not least, non posso non ringraziare il mio coinquilino speciale Fabio, che ha dovuto sopportare tutto lo stress che non ho mai fatto conoscere ad altri, mangiare cibo insipido e pure lavare i piatti, e nonostante tutto continua a volermi bene e a ritenersi fortunato.

I acknowledge the Italian Institute of Technology and Regione Autonoma della Sardegna for financial support through SEED project "POLYPHEMO" and L.R. 7/2007, project "Nanomateriali eco-compatibili per celle fotovoltaiche a stato solido di nuova generazione CRP-24978", respectively.

CONTENTS

ACRONYMS

PV photovoltaic

PCE power conversion efficiency

DSSC dye-sensitized solar cells

UV ultra-violet

P3HT Poly(3-hexylthiophene)

nT oligothiophene

SWNT single-walled carbon nanotubes

NIR near-infrared

DFT density functional theory

XC exchange-correlation

LDA local density approximation

GGA generalized gradient approximation

TDDFT time-dependent DFT

MPMD Model potential molecular dynamics

vdW van der Waals

BHJ bulk heterojunction

2T bithiophene

4T quarterthiophene

6T sexithiophene

Part I

INTRODUCTION

1 INTRODUCTION

Contents

1.1 TECHNOLOGICAL BACKGROUND - NOVEL NANOMATERIALS FOR PHOTOVOLTAICS

Sunlight conversion through photovoltaic (PV) effect represents one of the most viable methods to produce energy in a sustainable way. However, although the availability of solar energy is ideally infinite, the solar energy striking the earth being about 120,000 TW[1], our capability to exploit it is definitely depending on the efficiency of PV systems. The latter varies greatly depending on the materials and on the technology employed, and usually efficient systems are related to high cost and/or scarce availability of raw materials. First generation PV systems, such as single crystal silicon based devices, exhibit efficiencies around 20% (record 27.6%[2], see Fig. 1), but suffer from high cost of manufacturing and installation[3,4]. The second generation devices, usually called thin-film solar cells, are made from layers of semiconductor materials a few micrometers thick. The materials used for the production of this type of cells include amorphous silicon, cadmium telluride (CdTe), and copper indium gallium diselenide (CIGS). The combination of using less material and cheaper manufacturing processes allows to build panels at lower cost, but their production requires the use of very rare materials[5,6]. This technology has not yet accomplished a signficant impact on the PV industry[7]. The so-called third generation PV are the ultimate frontier of solar energy research, and promise to deliver high efficiencies at an

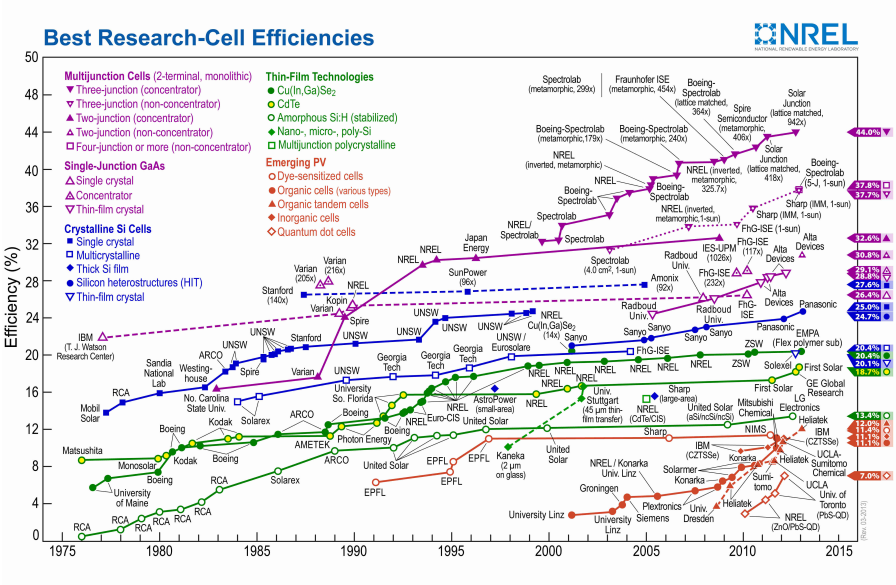

Figure 1: Research cells efficiency record chart (downloaded on March 27, 2013 from Ref.[2])

Third generation photovoltaics

economically viable cost. Third generation devices are strongly based on nanotechnology and are made from a variety of new materials besides silicon, including nanotubes, quantum dots, organic dyes and conductive plastics. These systems are quite cheap not only because of the low price of the raw materials, but mostly because they can be easily synthesized with very economic techniques. For example, colloidal synthesis[8,9] can be employed to obtain solar inks, which can then be easily deposited on suitable substrates using conventional printing technologies[10,11]. Conductive and semiconducting organic materials can be seen as alternative cheap materials for the production of organic and hybrid third generation PV[12,13]. Furthermore, most organic compounds are environmentally friendly and, in contrast to conventional silicon cells, their production or disposition is not a polluting process. In particular, conjugated polymers are an important class of organic hole conductors and electron donors which are used in third generation photovoltaics in association with carbon fullerenes[12,14], nanotubes[15], titanium dioxide[16], zinc oxide[17] etc. as the basis for organic and hybrid electronic devices.

1.1.1 *Organic and hybrid systems*

Fully organic devices

Among third generation solar cells, organics have shown an impressive progress in recent years[7,18–21]. Organic solar cells are characterized by the use of organic materials both in the p- and in the n-type part of the device. Poly(3-hexylthiophene) (P3HT) is one of the most used electron donors in polymer-based solar cells[10,22,23], for example in conjunction with carbon fullerenes[18]: it is a conjugated polymer which is able to absorb light in the visible spectrum and provides a very high hole mobility among organic semiconductors (around 0.1 $cm^2V^{-1}s^{-1}$ [24]. Typical mobilities in conjugated polymers are below $10^{-2}cm^2V^{-1}s^{-1}$ [25,26], much lower than in crystalline silicon, where it is about 1000 $cm^2V^{-1}s^{-1}$). Hole and electron mobility is important in such devices since the carriers are more likely to recombine if they do not reach the electrodes before separating. The transport in fullerene acceptors (which are zero-dimensional structures) is based on hopping, that gives rise to a limited mobility[27,28].

SWNT-polymer systems

Thus, since one-dimensional single-walled carbon nanotubes (SWNT)s exhibit very high electron mobility[29,30] (around 10^5 $cm^2V^{-1}s^{-1}$ [31], higher than in crystalline inorganic semiconductors) their use as electron acceptors has been proposed as an alternative to carbon fullerenes. Furthermore, the light absorbance of SWNTs can be widely tuned throughout the visible and near-infrared (NIR), a feature which could increase the percentage of absorbed photons[28]: it has been demonstrated[32] that the photons absorbed by SWNTs contribute to the photocurrent in polymer-based PV devices, extending the absorption spectrum to the NIR. However, the power conversion efficiency (PCE) of such P3HT-SWNT systems is still very low, reaching 0.5% in 2008[33]. An important limiting factor is represented by the complex nature of SWNTs samples, which are normally composed by both semiconducting and metallic nanotubes, of different chirality and diameter. Understanding which types (semiconducting, large/small diameter etc.) of nanotubes are more suitable for polymer-based solar cells is crucial, and, furthermore, the preferred types shoud be easily selected and separated from the others to optimize the device performances. Despite the great progress in selective growth methods[34–37], further improvements are still needed in this direction. Postgrowth separation through polymer wrapping is an alternative technique which has attracted much attention in the last decade[38–41]. It consists in dispersing the SWNTs

in a solution containing a material (often a conjugated polymer) which selectively coats the (for example) semiconducting nanotubes separating them from their metallic counterparts.

Hybrid systems

Better control on the semiconducting properties of the elecron acceptor can be achieved by using metal oxide nanostructures instead of organic ones in combination with polymers, so forming hybrid donor-acceptor systems. The most commonly used metal oxides for hybrid solar cells are ZnO and TiO_2. These inorganic materials can be easily synthesized in different nanostructures[42–44] and their electronic properties can be tuned by controlling the size and the shape of the nanoparticles[45,46]. An additional advantage of the use of inorganic nanostructures with respect to organic acceptors is that the charge carrier mobility (e.g. around 700 $cm^2/(V \cdot s)^{-1}$ for bulk ZnO[47]) can be improved by increasing the crystallinity of the material or doping[48]. Furthermore, hybrid cells have potentially higher lifetimes: metal oxides in fact are stable materials compared to organic compounds, which can be degraded by elevated temperatures, exposure to oxygen[49], water[50] and ultra-violet (UV) light[51,52]. In particular, the exposure to UV light is an important issue in a solar cell. Since ZnO and TiO_2 exhibit pronounced absorption in the UV range (ZnO and TiO_2 have a band gap of 3.3[53] and 3.05[54] eV, respectively), they can act as filters for the organic material in the hybrid cell thus protecting the more sensitive part of the device.

Dye-sensitized solar cells

Among hybrid solar cells, a successful example is represented by the so-called dye-sensitized solar cells (DSSC): they are ternary systems in which an organic dye plays the role of light absorber, while the hole and electron transport are performed by two different materials. Such devices are possible in both liquid and solid state form. Liquid state DSSC consist of a porous nanocrystalline film (typically of TiO_2 nanoparticles) sensitized by an anchored organic dye and completed by a redox elctrolyte[55–57]. In these cells, the nanocrystalline films collects the photogenerated electrons while the redox electrolyte is responsible for the collection of the holes[55]. Conversely, in solid state DSSC the liquid electrolyte is replaced by room temperature molten salts, inorganic p-type semiconductors, ionic conducting polymers and organic hole transport materials[58,59]. The disadvantages of such solar cells are the limited choice of suitable hole collectors[60] and their lower efficiency with respect to liquid state DSSC (10.2%[61] vs 12.5%[62] PCE).

A promising solid state hybrid technology uses colloidal lead chalcogenide nanocrystals[9,63] as electron acceptors, in combination with different polymers as electron donors[64]. These devices show among the highest PCE for hybrid solid-state solar cells, reaching 2.9% in 2012[9]. However, the use of non-environmentall-friendly materials such as lead poses again the problem of device disposition after use. More eco-friendly hybrid solar cells can be easily obtained from solution by mixing conductive polymers such as P3HT with biocompatible materials such as e.g. ZnO[46,65,66], which can be easily synthesized into nanostructures[42–44]. Hybrid ZnO-P3HT devices have been created by mixing the polymer with ZnO nanoparticles of different shape[22,67–69] (see e.g. Fig.2). In particular, ZnO nanoneedles grown perpendicularly to the substrate have attracted interest since they can be easily synthesized from solution at low temperature[70,71]. However, the state-of-the-art efficiency of ZnO-P3HT hybrid solar cells is still lower than in all-organic systems[65,66,72]. As P3HT and ZnO taken separately possess all the required characteristics to give rise to good performances in solar cells, the reason of such a low efficiency must be found in atomic scale features of the ZnO-P3HT nanostructured interface, that deserves better theoretical understanding[72].

Eco-friendly systems

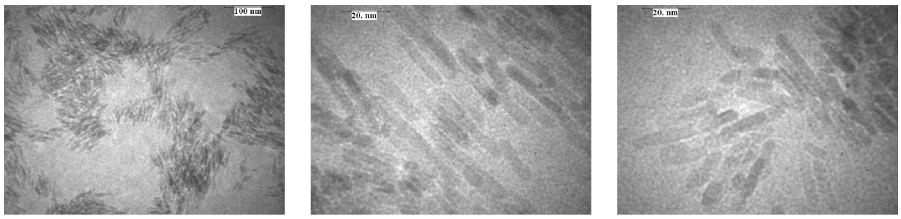

Figure 2: Transmission electron microscopy image of a ZnO-P3HT blend. Adapted from Ref.[65].

1.2 PHOTOCONVERSION IN DONOR-ACCEPTOR HYBRID NANOSTRUCTURES

The conversion of sunlight into electricity by the photovoltaic effect in conventional p-n junction solar cells consists of the following steps: a photon is absorbed by the device and, if its energy is greater than the band gap energy (E_g), an electron is promoted from the valence to the conduction band, leaving an excess hole in the valence band. The built-in voltage of the p-n junction drifts the electron and the hole towards

opposite directions, and if the junction is connected to an external load, a flow of current is observed. While in inorganic

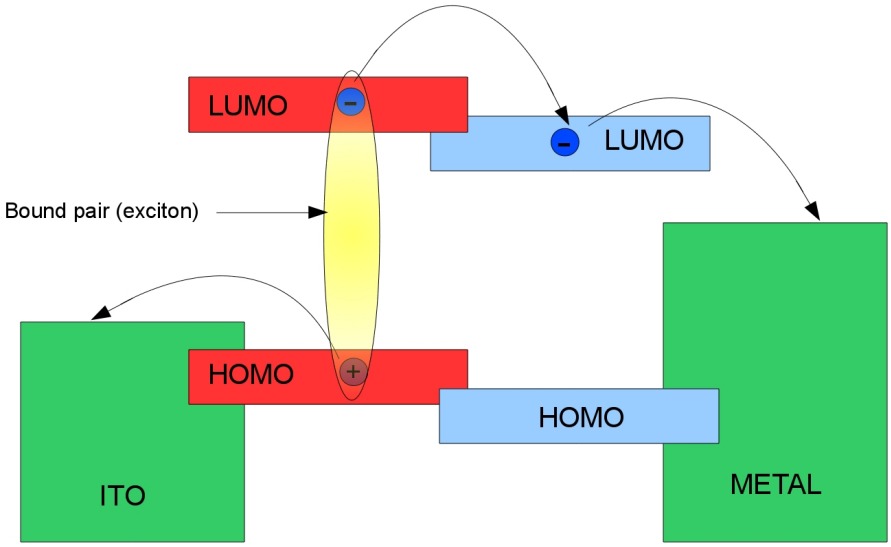

Figure 3: Photoconversion in a donor-acceptor system.

semiconductors (such as silicon) photoexcitation leads to free (or slightly bound) charge carriers, in organic semiconductors strongly bound electron-hole pairs (excitons) are created. The charge generation in these systems can be summarized in a three-steps process: first the electron-hole pair is created by photoexcitation, then the exciton is separated into free carriers, which are eventually delivered to the electrodes and to the external circuit to generate a photocurrent (see Fig.3). Charge separation in organic semiconductors takes place at the interface between an electron donor (p-type) and an electron acceptor (n-type) material[73]. A critical requirement for photovoltaic applications is that the interface corresponds to a type-II (staggered) junction in order to get an efficient charge separation (see Fig.3). If the exciton is generated in the donor material, the energy needed to break the excitonic bond is approximately given by the offset between the lowest unoccupied molecular orbitals (LUMO) of the electron donor and of the electron acceptor. Conversely, in the case of an exciton generated in the acceptor material, the offset between the highest occupied molecular orbitals (HOMO) will provide the energy needed for dissociation. Thus, the bound pair must diffuse in the device until such an interface is found.

1.2.1 *The bulk heterojunction*

Since the exciton lifetime is very limited (e.g. 0.4 ns in P3HT[74]), to ensure a high quantum efficiency the donor-acceptor interface must be met in the first few nanometers from the site in which the exciton has been generated. For this reason, the so-called bulk heterojunctions have been developed, in which the p- and n-type materials are intimately mixed on a nanometer scale and allow for a higher contact surface between the two (see Fig.4). These junctions are typically created by dispersing n-type nanoparticles into a polymer matrix, or by infiltrating the polymer into a nano-sized acceptor network[75,76]. However, since after charge separation the carriers must reach the electrodes, a continuous conductive path must exist which can be followed by electrons and/or holes towards the external circuit. Charge recombination is in fact a major loss mechanism in the cell, and the carriers are likely to recombine if they do not reach the electrodes as faster as possible. Because of this, the degree of intermixing in organic solar cells cannot be arbitrarily large, since in highly intermixed compounds part of the electron/hole conductor is no longer connected to the collecting electrodes, preventing part of the charges formed to contribute to the photocurrent[72]. Morphological features of the

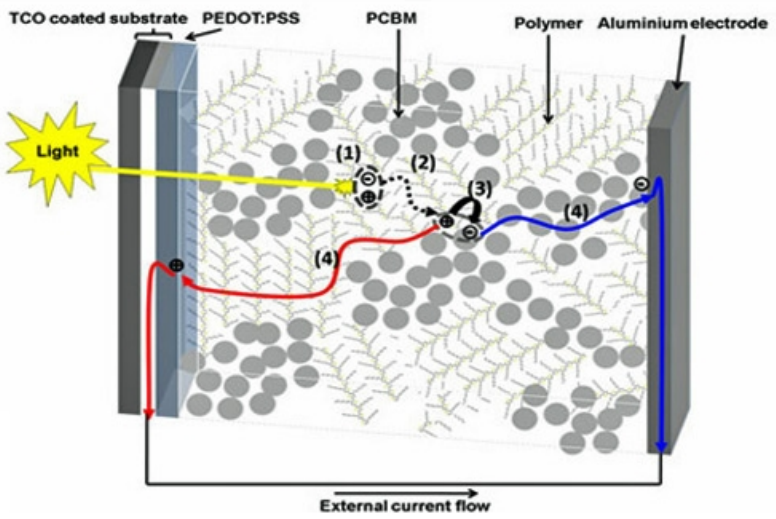

Figure 4: Bulk heterojunction architecture.

donor-acceptor blend at the nanocurved interface are of particular importance since they strongly influence charge separation

Ordered heterojunctions

and transport. Ideally, one would have an ordered heterojunction, in which the two moieties are assembled in such a way to favor the carrier transport. It is more difficult to fabricate an ordered structure than a disordered blend, but the advantages of order are evident. At first, in an ordered structure the size of both phases can be controlled to ensure that, regardless of where the exciton is generated, an interface is met within an exciton diffusion length. Then, after dissociation the electrons and holes have straight pathways to the electrodes, which favor that the carriers escape the device as quicker as possible, minimizing recombination. Furthermore, in an ordered structure it is in principle possible to align conjugated polymer chains, increasing the mobility of their charge carriers: it is known for example that the transport properties of P3HT are better when the polymer is in its crystalline phase[77–79]. Aligning the polymer chains onto the substrates, however, is still a major challenge in polymer research. Typically, in ordered heterojunctions the acceptors are elongated nanostructures, such as carbon nanotubes or metaloxide nanorods/nanoneedles. For example, polymer/nanotubes blends are typically synthesized by dispersing the nanotubes into an acqueous solution containing the polymer[80]: the polymer coats the hydrophobic nanotubes surfaces and disassociates them from the aggregate form[81]. At the nanoscale the coating corresponds to a complex organization of the polymer chains on the nanotube surface. In particular, analyzing SWNTs with diameters as small as 1.5 nm by Scanning Tunneling Microscopy, it has been observed that single P3HT chains can arrange into pseudo-helical configurations with arrangements depending on the nanotube chirality[82] (see Fig.5). If the nanotubes are completely wrapped by polymer chains, they will be isolated from each other and a continuous conductive path for the electrons will not be possible anymore. Several features still need to be clarified for such polymer-nanotubes systems. The observed pseudo-helical structure observed for P3HT on SWNTs is still not understood and, since such blends operate in solvent-free environment, understanding at the atomic-scale the stability of the wrapped configuration once the solvent has been dried could aid the design of highly oriented systems with improved conducting properties.

Polymer wrapping

P3HT-ZnO blends

Similar considerations are valid also for hybrid blends formed by P3HT and ZnO nanoneedles. Given the geometry involved, also these systems are likely to show wrapped con-

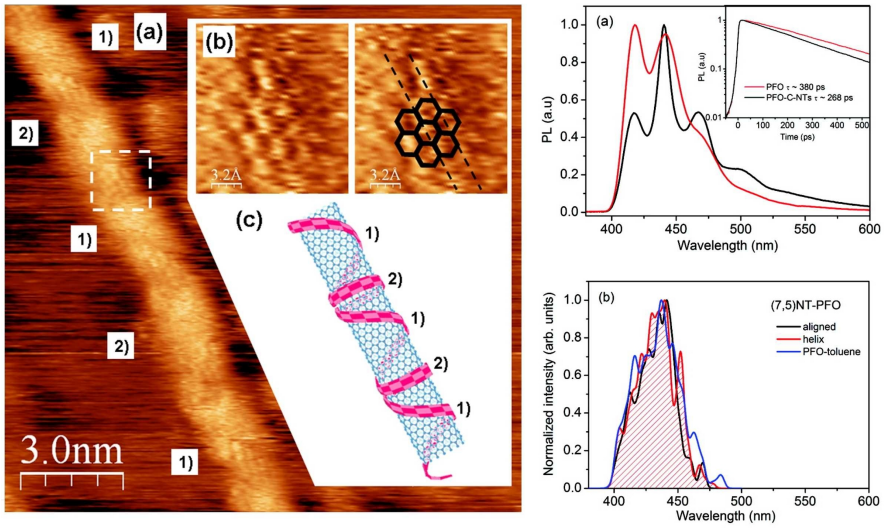

Figure 5: Left: Scanning Tunnel Microscopy image of a P3HT chain wrapped around a carbon nanotube. Adapted from Ref.[82]. Right: comparison between experimental and simulated photoluminescence spectra of poly(9,9-dioctylfluorenyl-2,7-diyl) (PFO)/carbon nanotubes complexes. Adapted from Ref.[83].

figurations of the polymer chains. It has been experimentally found that the P3HT tends to be amorphous rather than crystalline at the interface with planar ZnO surfaces[17,84], but the actual morphology of this polymer on ZnO nanostructures is still unknown.

The nanostructuration has also great impact on the optoelectronic properties of the systems of interest. At first, for inorganic nanoparticles, it is known that the optical properties are strongly dependent on their shape and size through quantum confinement effects[45,46]. Furthermore, the morphological features induced in the polymer conformation by the nanostructured substrate affect its optolelectronic properties[85–87]: for example, it has been shown that wrapped or aligned polymer chains exhibit different emission spectra[83] (see Fig.5), and that the band gap of disordered P3HT chains is larger than in planar chains with no disorder[88]. The donor/acceptor electronic band gaps and their energy-level alignment are fundamental for designing systems with the desired optoelectronic behavior[89]. In particular, the alignment is often deduced from the electronic ground states of the donor and acceptor in their isolated form. However, this simplification neglects their mutual

interactions which involve electronic polarization and may include charge transfers between the two[90]. A consequence of these interactions is the formation of interface dipoles at the interface, whose magnitude depends on the geometry of the complex[91,92]. The presence of an interfacial dipole can produce a significant shift of the electronic energy levels of both components[90]: the same materials thus can provide different alignments in bilayer architectures or bulk heterojunctions, depending on the interfacial morphology[92–94].

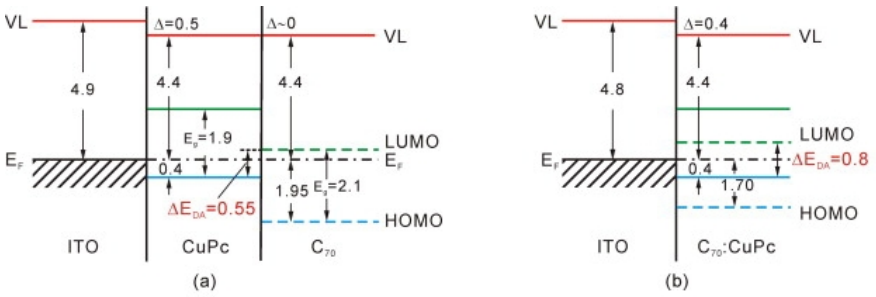

Figure 6: Energy-level alignment of (a) C_{70}/CuPc bilayer and (b) a C_{70}/CuPc bulk heterojunction.The molecular levels of CuPc are presented in solid line, while that of C_{70} in dashed line. Adapted from Ref.[94].

1.2.2 *Methodological concerns*

Despite the recent progress in experimental characterization techniques, including atomic force microscopy and positron annihilation spectroscopy (see e.g Refs. 72 and 95), accurate description of interfaces is challenging due to the difficulty of measuring properties at the nanometric scale. In this direction, atomistic simulations are emerging as an important tool for understanding and predicting the interfacial morphology and optoelectronic properties of the hybrids. From the theoretical point of view, however, hybrid interfaces are a complex subject. At first, in bulk heterojunction (BHJ) systems the configurational complexity of organic and inorganic components (molecules and nanoparticles) requires to study systems of large size which cannot be fully treated by ab initio methods. Furthermore, if one whishes to take into account the effects of the synthesis procedure of BHJs, thermodynamic effects begin to be important requiring long simulation runs at finite temperature. Model potential molecular dynamics (MPMD) is a suitable

computational tool for the simulation of such systems, since it allows to consider large sizes and long times, several order of magnitude larger than ab initio methods. This technique is widely used in different fields, such as biophysics (e.g. drug design[96,97]), study of mechanical behaviour of brittle materials[98,99], thermal transport modeling[100] and so on. The use

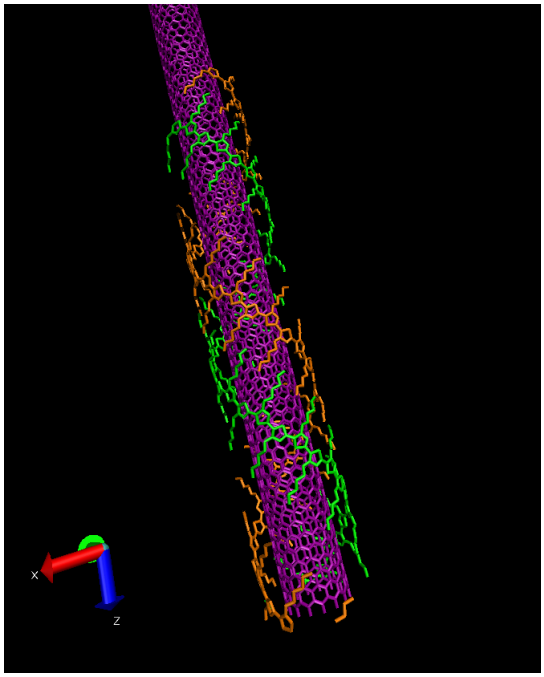

Figure 7: Snapshot taken from a MPMD simulation of a carbon nanotube wrapped by two P3HT chains.

of MPMD for describing hybrid organic/inorganic interfaces instead is less common, mainly because of the scarce availability of model potentials for treating hybrid interactions. Recently, an increasing number of works have been published which make use of MPMD to study hybrid systems. For example, it has been applied to study the thermal expansion of polyimide-SiO_2 nanocomposites for applications in microelectronics[101], while the effects of the presence of inorganic titanate nanotubes in poly(dimethylsiloxane) rubbery membranes has been investigated through a combined experimental plus MPMD approach[102]. Regarding more PV-oriented hybrid systems, the adhesion of polythiophenes on TiO_2 has been studied and the role of the curvature has been highlighted[103,104]. Planar ZnO-P3HT interfaces have been examined as well[105], confirming the experimental evidence of polymer disorder at the ZnO interface. On the other hand, the effects of curved ZnO-P3HT inter-

faces have not been investigated so far, despite they correspond to important characteristics emerging at the nanoscale.

If electronic properties are of interest, MPMD, which does not take into account any electronic effects, must be supported by electronic structure calculations. However, also for ab initio hybrid interfaces are challenging. First, accurate description of the band gap of metaloxides cannot be achieved in the framework of density functional theory (DFT) by using standard LDA and GGA functionals[106,107]. The use of hybrid functionals has proven to give better results, but the computational load required is sensibly higher[108]. For confined systems, the so-called ΔSCF method[109] can be employed, which gives accurate results on the quasiparticle (QP) energy levels[110–112]. Furthermore, in these systems the donor-acceptor adhesion involves both covalent and dispersive van der Waals (vdW) interactions. If the covalent term dominates, DFT methods can efficiently model the hybrid structure (see e.g. Refs.[113,114]), but since vdW energy originates from the correlate motion of electrons, accurate description of dispersive vdW interactions would require the use of many-body quantum mechanics methods[115]. However, use of these methods is only feasible for systems containing a very small number of atoms, thus full ab initio calculations of vdW forces on systems of reasonable size is not possible at present. Several methods have been developed to include dispersive forces in DFT calculations, some of them at no additional computational cost. Dion et al.[116], for example, have proposed a van der Waals density functional (vdW-DF) method to include the vdW interactions, which calculates the vdW exchange-correlation energy by mixing generalized gradient approximation (GGA) exchange, local density approximation (LDA) correlation and a long-range nonlocal correlation energy derived from a series of different approximations. The computational cost of this method is comparable to DFT-GGA, but its accuracy for solids has not been yet fully established[115]. A different approach is represented by the DFT-D methods, which take into account vdW interactions by simply adding the interatomic dispersion energy contributions to DFT total energies, modeled by a C_6R^{-6} potential[117–119]. The major drawback of this approach is its empirical nature, which requires at least two fitting parameters per atomic element. However, application of this dispersive correction has given good results for many intermolecular interaction, and it can be connected to different functionals[117].

1.3 SCOPES AND AIMS OF THIS THESIS

The aim of the present thesis is to understand the effects of the nanostructured shape of organic and inorganic materials on both the morphology and the optoelectronic properties of hybrid and organic interfaces. More specifically, we want to address the following points:

- From the morphological point of view

  Generate realistic atomistic models of hybrid and organic interfaces between the conductive polymer P3HT and a series of nanostructured electron acceptors, namely ZnO nanoneedles/nanoclusters or SWNTs

  Understand how a single polymer chain organizes itself onto a one-dimensional acceptor nanostructure, such as a ZnO nanoneedle or a carbon nanotube

  Identify how the curved nanostructured shape affects the chain adhesion and, more in general, the polymer-substrate interactions

  Study the thermodynamic stability of the observed polymer conformations under different conditions (temperature, chain length, density)

- From the electronic point of view

  Calculate the electronic-level alignment of the hybrid by including the actual shape, curvature and morphology of the acceptor, in comparison with the case of a planar interface

  Understand how the optical absorption properties are correlated with the nanoscale morphology

The first point is elucidated in Chapters 2 and 5, where the P3HT wrapping on ZnO nanoneedles and carbon nanotubes is studied by MPMD. In particular, in Chapter 2 the effects of the nanoneedle shape on the polymer-nanoneedle adhesion are explained. The thermodynamic stability of the donor-acceptor system is also studied at finite temperature. Chapter 5 presents a morphological analysis of P3HT wrapping on SWNTs of different chirality in vacuo. The wrapping is studied thoroughly for a wide range of temperatures and for realistic polymer lenghts via MPMD simulations.

The electronic properties and the second set of problems are addressed in Chapters 3 and 4. The electronic level alignment

of an hybrid system composed by a $(ZnO)_{60}$ nanocluster and several polythiophene molecules is calculated in Chapter 3 in the framework of the ΔSCF method. In Chapter 4 we calculate the absorption spectra of a set of $(ZnO)_{60}$ isomers with the aim to give a theoretical support to aid the identification of the actual configuration of the $(ZnO)_{60}$ nanocluster. Time-dependent DFT is employed for these calculations.

Part II

RESULTS

2

POLYMER WRAPPING ON ZNO NANONEEDLES

Contents

2.1 INTRODUCTION

Bulk heterojunctions, in which the electron donor and acceptor are intimately mixed forming a nanosized interpenetrating network, are often synthesized from solution[22,120], and while it is possible to accurately tune the size and shape of the inorganic nanoparticles by the synthesis procedure[45,46], controlling or even characterizing experimentally the donor/acceptor interface is still an open issue. In this Chapter we consider a model system for the study of the adhesion of P3HT on one-dimensional ZnO nanostructures, which consists in a single P3HT chain wrapped on a ZnO nanoneedle. This model is representative of the interface between the polymeric electron donor and the inorganic acceptor when the latter is nanostructured. By using MPMD, we study the adhesion of the P3HT chain on the ZnO nanoneedle for different chain organizations. In particular, we study helically wrapped polymer conformations and we give an analytical model for the polymer adhesion on the nanoneedle for different coiling angles. The importance of taking into account wrapped configurations can be understood by considering a simple model based on physical intuition: as schematically depicted in Fig. 8, assuming an attractive interaction between a long polymer molecule and the nanoneedle, the initial relative position during the formation of the donor-acceptor assembly controls the geometry of the hybrid. If the polymer backbone is initially parallel to the nanoneedle axis (a), the interaction between the two will keep the polymer chain aligned. Otherwise, if the initial configuration of the

separate moieties is tilted (b), the polymer will likely wrap around the nanoneedle in order to maximize the interaction. The final conformation of the polymer-nanoneedle interface will depend on the full synthesis procedure. For this reason, limiting the study to the calculation of the lowest energy structure cannot be exhaustive to determine if wrapped configurations are possible for P3HT on ZnO nanoneedles. Thus, we further studied the stability of the wrapped configurations at finite temperature, providing evidence that they are stable at room temperature because of the low mobility of the polymer on the ZnO surface. This result must be taken into account when designing nanostructured P3HT-Zno systems.

Most of this Chapter has been taken from *C. Caddeo et al., J. Phys. Chem. C 115 (2011)* (Ref. 121.)

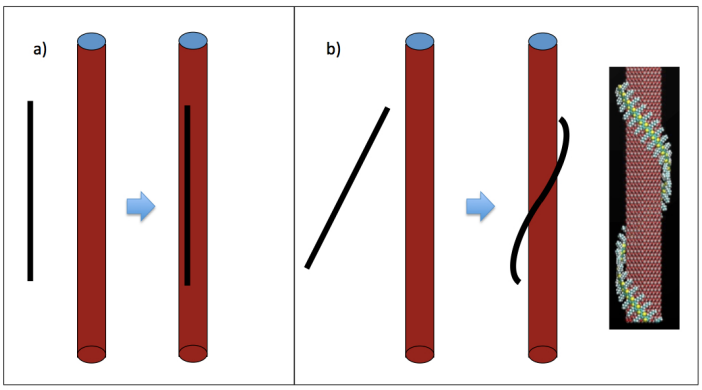

Figure 8: Schematics of the adhesion of a long polymer chain on a ZnO nanoneedle. If the polymer backbone is initially parallel to the nanoneedle axis (a), the final configuration will be aligned. If the polymer backbone is initially tilted with respect to the nanoneedle axis (b), the polymer will wrap around the nanoneedle to maximize the interaction.

2.2 SYSTEM DESCRIPTION

The object of the present study are ZnO wurtzite-structured nanoneedles, with hexagonal cross-section, and grown along the [0001] direction with $(10\bar{1}0)$ facets. They are ideally infinite in length (due to periodic boundary conditions) and have a diameter as small as $\sim$ 2.5 nm. ZnO nanoneedles of this diameter have been produced experimentally from solution[122]. The simulation cells have dimensions of 7 nm $\times$7 nm $\times$21.3

nm, along the x, y and z directions, respectively. The P3HT molecules are up to 64-monomers (mon's) long (~ 24 nm). This length is smaller than the typical experimental one[123], but it is large enough to allow easy bending and wrapping around the nanoneedles by limiting the system size and consequently the simulation time. The simulations cells contain ~ 12000 atoms. All the computational details are described in the Appendix section (Chapter A).

2.3 RESULTS AND DISCUSSION

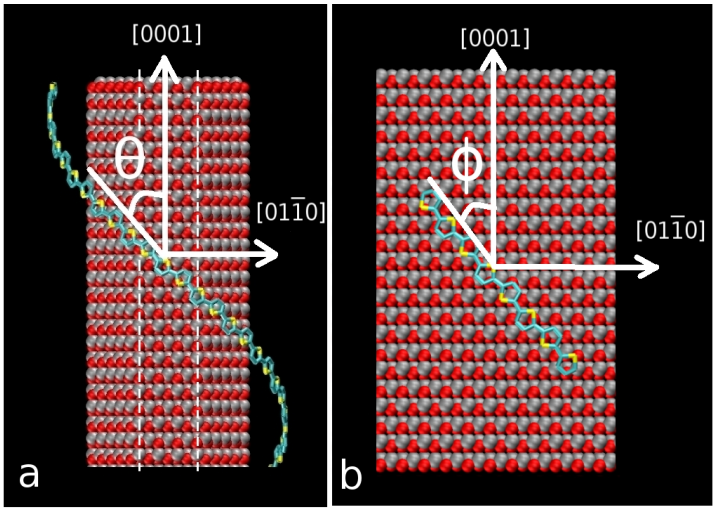

Figure 9: (a) Definition of coiling angle around the nanoneedle and (b) rotation angle on the planar surface. Dashed lines in (a) are a guide to the eye to identify the nanoneedle facets. Note that only the backbone atoms of the polymer are shown for clarity.

The typical initial configuration for the following MD simulations is represented in Fig. 10 (top panels). It consists of a ZnO nanoneedle and a helical-shaped polymer chain wrapped around ZnO. In order to explore the most favorable configurations, the arrangement of the polymer on the nanoneedle was varied by studying regular helices. Each helix is characterized by the coiling angle θ (defined as in panel (a) of Fig. 9), with $10^\circ \leqslant \theta \leqslant 70^\circ$. Each system only differs from the others for the coiling angle. The corresponding structures were first relaxed and then annealed at room temperature for ~ 3 ns. Two exam-

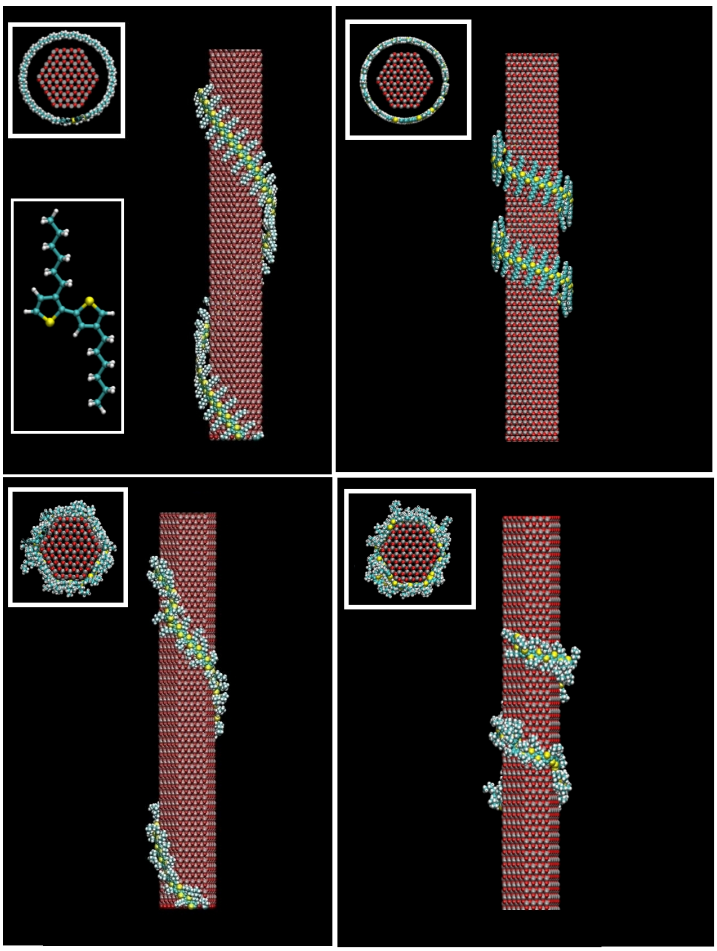

Figure 10: Example of starting (top) and final (bottom) configurations for two different systems. On the left, the coiling angle is 40°, on the right 70°. The insets show the top view of the systems and the chemical structure of P3HT. In all figures, red is Oxygen, grey is Zinc, cyan is Carbon, yellow is Sulphur and white is Hydrogen.

ples are reported in Fig. 10 (bottom panels). Upon annealing, the polymer bends around the nanoneedle following its hexagonal section (see insets in bottom panels of Fig. 10). The flexible hexyl tails of the polymer are largely distorted with respect to the ideal regioregular geometry (compare top and bottom panels of Fig. 10), as a result of the local electrostatic interactions between the partial charges of the chain and the surface ions.

The binding energy of the hybrid system, $U^{N}{}_{B}(\theta)$, where N stands for "nanoneedle" and B stands for "binding", is defined as the difference between the total energy of the bound configuration $U^{N}{}_{ZnO+P3HT}(\theta)$ and the total energy of two separate

components (U^N_{ZnO} for the ZnO nanoneedle and U^0_{P3HT} for the straight (0) isolated polymer, respectively). All the energies were taken after relaxing the structures for 50 ps at $T = 0$ K.

$$U^N_B(\theta) = U^N_{ZnO+P3HT}(\theta) - U^N_{ZnO} - U^0_{P3HT} \quad (1)$$

where the θ-dependence is introduced by the sole $U^N_{ZnO+P3HT}(\theta)$ contribution. The calculated $U^N_B(\theta)$ values are reported in Fig. 11 (filled symbols) as a function of the coiling angle (top scale). The dotted line will be described later.

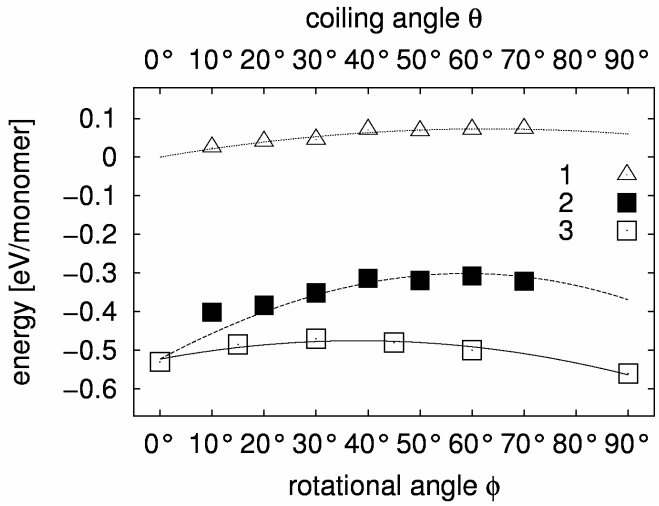

Figure 11: Chain strain energy (open triangles - 1) and polymer-nanoneedle binding energy (filled squares - 2) as a function of the coiling angle (top scale). Polymer-surface binding energy (open squares - 3) as a function of the rotational angle (bottom scale). Lines are numerical fit (see text).

The behavior is non-monotonic with the highest binding energy occurring at small coiling angles, and it means that the straight polymers are more strongly bound to the nanoneedle. Here, in order to separately account for all the possible contributions to the configurational energy of an isolated wrapped polymer, the same conformation of the polymer obtained for the relaxed hybrids was considered, and then the resulting total energy $U_C(\theta)$ of the molecule in its present helical conformation was calculated. The configurational energy difference $U_C(\theta) - U^0_{P3HT}$ is shown in Fig. 11 (open triangles) where it is also fitted by a second-order function of the coiling angle θ (dotted line)

$$U_C(\theta) = \alpha_C \theta^2 + \beta_C \theta \quad (2)$$

Fitting parameter	Value
α_C	$-1.84 \cdot 10^{-5}$[eV/mon]
β_C	$2.32 \cdot 10^{-3}$[eV/mon]
α_P	$-3.28 \cdot 10^{-5}$[eV/mon]
β_P	$2.5 \cdot 10^{-3}$[eV/mon]
γ_P	-0.52[eV/mon]
A^P	10249.39 [eV]
$d^P{}_0$	0.31 [Å]
C^P	879.52 [eV·Å^6]
A^E	4308.98 [eV]
$d^E{}_0$	0.36 [Å]
C^E	1105.52 [eV·Å^6]

Table 1: Values of the fitting parameters

where α_C and β_C are fitting parameters (values are reported in Table 1).

This is consistent with the quadratic dependence of the polymer strain energy on the local curvature as reported elsewhere[103]. $U_C(\theta) - U^0{}_{P3HT}$ increases by a fairly small amount in the range $0 \leqslant \theta \leqslant 70°$ (actually from 0 to 0.07 eV/mon). At variance, in the same range the binding energy $U^N{}_B$ given in Eq. 1 gives a larger variation of 0.25 eV per monomer, suggesting that other contributions must be considered to be added to simple coiling.

A new feature not considered so far comes from the relative orientation of the polymer backbone with respect to the crystalline substrate. The adhesion of a straight P3HT segment on a ZnO planar surface (P) was then calculated as a function of the molecular orientation. This is defined by the rotation angle ϕ formed by the polymer backbone and the [0001] direction (see Fig. 9, right panel). The corresponding energy $U^P{}_B(\phi) = U^P{}_{ZnO+P3HT}(\phi) - U^P{}_{ZnO} - U^0{}_{P3HT}$ (where $U^P{}_{ZnO}$ is the total energy of the planar ZnO surface) is reported in Fig. 11 by open squares. When the P3HT backbone is aligned to the

$[01\bar{1}0]$ direction (corresponding to $\phi = 90°$) the binding is maximum, corresponding to $U^P{}_B(\phi = 90°) = -0.56$ eV/mon. The calculated energies can be fitted by a simple quadratic function

$$U^P{}_B(\phi) = \alpha_P \phi^2 + \beta_P \phi + \gamma_P \tag{3}$$

where α_P, β_P and γ_P are fitting parameters (values are reported in Table 1).

This analysis provides evidence that the ϕ-dependence must be included in the binding energy of the P3HT on the nanoneedle. When considering a wrapped polymer chain, the average rotation angle on the facets depends on the coiling angle, i.e., $\phi = \phi(\theta)$. For the case of a regular helix considered here, $\phi = \theta$ and we can therefore replace ϕ with θ everywhere. If applied alone, the anisotropy argument would predict the largest binding at $\theta \sim 90°$, i.e., when the polymer chain is orthogonal to the growth direction of the nanoneedle. This is not the case for $U^N{}_B$ which includes other contributions. For example, as discussed above, the polymer strain favors small coiling angles.

Although a better physical insight is provided by the above argument, a model for $U^N{}_B(\theta)$ only including contributions from coiling and relative orientation features ($U^P{}_C(\theta)$ and $U^P{}_B(\theta)$, respectively) is still unable to fully account for the calculated binding energy; as a matter of fact, it is possible to estimate $[U^P{}_C(\theta) + U^P{}_B(\theta)] - U^N{}_B(\theta) \sim 0.1$ eV/mon, proving that a further correction is actually needed. A meaningful improvement consists in explicitly including the effects of the edges between the facets of the nanoneedle on the energetics of the problem. Edges are extended defects that affect the polymer adhesion. This is clearly shown by a simpler model system formed by just one thiophene molecule for which the binding energy is calculated on both a planar surface and a nanoneedle. In Fig. 12 such an energy is plotted versus the distance d between the center of mass of the molecule and the plane of the solid surface for three different configurations (shown in the top panels) corresponding to different symbols. It is found that the binding is favored when the thiophene interacts with the planar surface (empty squares) or with the center of a nanoneedle facet (empty triangles). Actually, the values are almost identical and can be fitted with the same curve (full line). Conversely, the binding is unfavored when the molecule is close to an edge (filled squares)

and the adhesion is reduced by $P^T{}_e \sim 0.13$ eV (dashed line). Both series of data can be fitted by Buckingham-type curves

$$E(d) = A \cdot \exp\left(-\frac{d}{d_0}\right) - \frac{C}{d^6} \tag{4}$$

where A^P, $d^P{}_0$ and C^P refer to the adhesion on the planar surface or on the nanonedle face, while A^E, $d^E{}_0$ and C^E correspond to the thiophene molecule close to the nanoneedle edge. Their values are reported in Table 1.

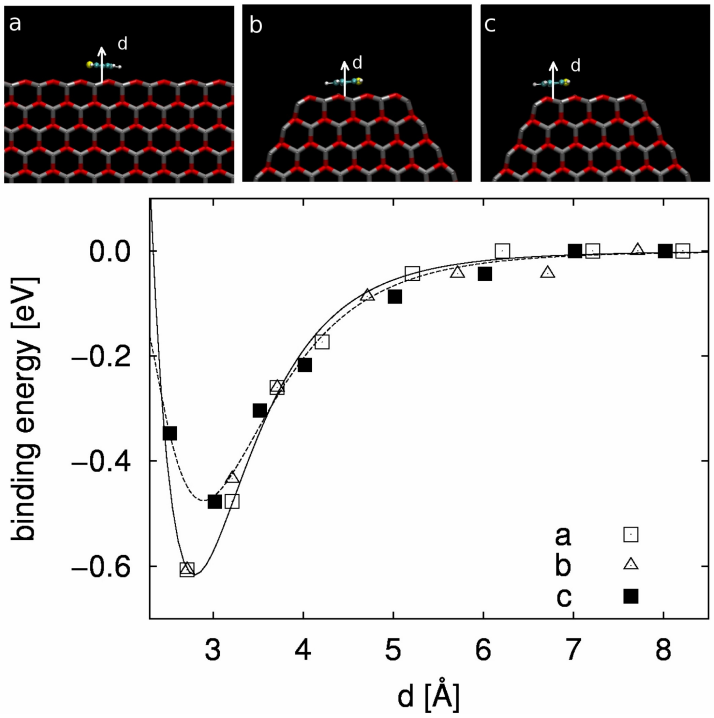

Figure 12: Top: snapshot of the investigated structures: (a) planar surface; (b) nanoneedle facet; (c) nanoneedle edge. Bottom: interaction basin of a thiophene ring on a ZnO planar surface (open squares), on a nanoneedle facet (open triangles), and on a nanoneedle edge (filled squares). The values are the minima amongst different rotational angles of the ring (on the ring plane) around its center of mass.

The above results for the single thiophene molecule can be extended to the case of the P3HT. Whenever a polymer is wrapped around a nanoneedle, some portions of the chain fall necessarily close to the edges of the nanostructure. According to the above analysis these portions of the polymer are less bound to the nanoneedle; the bigger the portion of chain close to the edges, the weaker is the binding.

The number of times N_{edges} the edges are met by the polymer depends on the coiling angle θ, and it is larger for larger coiling angles. A simple counting of N_{edges} can be obtained by dividing the polymer length L by the edge-to-edge distance $\frac{L_f}{\sin\theta}$ (where L_f is the facet width) along the coiling direction. We get

$$N_{edges}(\theta) \sim \frac{L}{L_f}\sin\theta \tag{5}$$

Eventually, a thorough expression is obtained for the the binding energy ${U_B}^N(\theta)$ including all the contributions

$${U^N}_B(\theta) = U_C(\theta) + {U^P}_B(\theta) + {P^N}_e N_{edges}(\theta) \tag{6}$$

where ${P^N}_e$ takes into account the reduction of the polymer adhesion energy due to the edges. ${P^N}_e$ is here used as an adjustable parameter. The best fit is reported as a dashed line in Fig. 11 for ${P^N}_e \sim 0.011$ eV, a value that is smaller than ${P^T}_e$ found for the single thiophene. This result suggests that the reduction of the adhesion of P3HT on the ZnO edges is smaller than in the case of a thiophene molecule. This is due to the fact that the polymer is flexible enough to optimize its morphology on the ZnO edge.

The analysis carried out at zero temperature shows that the P3HT chain is preferably aligned to the nanoneedle axis. Nevertheless, in real samples several factors such as solvent, thermal fluctuations, or synthesis procedures can induce wrapped configurations. In order to understand the stability of these configurations the nanoneedle-P3HT hybrids were also studied during annealings at $T = 300$ K and $T = 500$ K. The polymer morphology was not found to sizably evolve even after a 5 ns-long annealing. A fully unwrapping phenomenon is never observed both at room temperature or at T=500 K. This is in contrast with the case of P3HT on SWNT's, as described in Fig. 5. A comparison of the unwrapping process of the same polymer on a SWNCT or on a ZnO nanoneedle of similar diameter is presented in Fig. 13: the two systems only differ for the chemistry of the nanostructures. After 50 ps the polymer completely unwraps from the SWNT (bottom right), while the chains remain wrapped around the ZnO nanoneedle even after 7 ns (bottom left). It is important to remark here that the polymer adhesion on a nanoneedle (0.5 eV/monomer) is not much larger than in the case of a SWNT (0.4 eV/monomer). It is just the energy barrier for the polymer diffusion on the surface and for the unwrapping which is higher for the nanoneedle case. This is due

to the different nature of the polymer interaction with the ZnO surface including electrostatic forces not present in SWNT case.

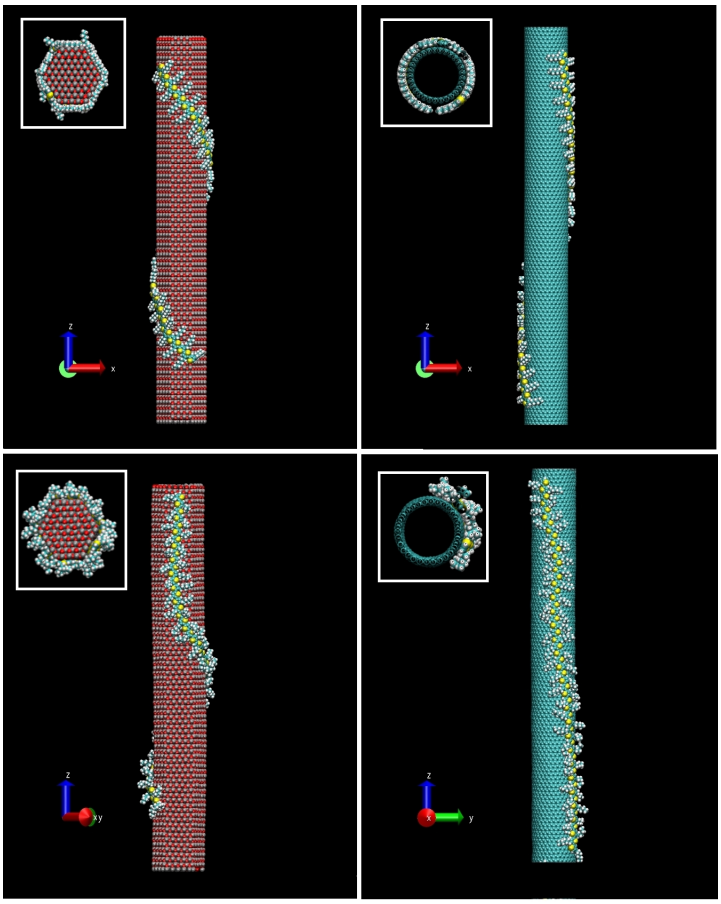

Figure 13: Left: starting (top) and final (bottom) configuration for a polymer-nanoneedle system annealed at T = 500K for 7 ns. Right: starting (top) and final (bottom) configuration for a polymer-SWNT system annealed at T = 500K for 50 ps. The insets show the top view of the systems.

2.4 CONCLUSIONS

In conclusion, by molecular dynamics simulations, the P3HT adhesion on zinc oxde nanoneedles was studied for different polymer configurations around the nanoneedle. The binding energy was shown to be a function of the polymer coiling angle, depending on the crystallography of the substrate onto which the polymer is adsorbed, the polymer chain strain and the presence of extended defects on the nanoneedle (edges). Though the most favorable configuration is the one in which the polymer is aligned to the nanoneedle, it is clear that wrapped configurations are stable at room temperature because of the low mobility of the polymer on the ZnO surface. At finite temperature such configurations are expected to occur with a probability $P(\theta) \sim exp(\frac{-\Delta E(\theta)}{k_B T})$ where $\Delta E(\theta) = U^N{}_B(\theta) - U^N{}_B(0) \simeq 0.1$ eV for $\theta < 30^\circ$ and they are expected to have an impact on the electronic properties of the hybrid interface, in particular as a result of the polymer curvature. This point will be discussed in Chapter 3.

3

ELECTRONIC PROPERTIES OF ZNO-OLIGOTHIOPHENES NANOSTRUCTURES

Contents

3.1 INTRODUCTION

In the previous Chapter we have discussed the effects of the presence of highly curved substrates on the morphology of the donor-acceptor interface. The curvature has also a strong influence on the optoelectronic properties of the system. For example, it has been shown that wrapped or aligned polymer chains exhibit different photoluminescence spectra[83]. This Chapter is focused on studying the electronic level alignment at the hybrid interface between a polymer chain and a ZnO nanostructure as the one described in Chapter 2. Since ab initio calculations are computationally more expensive than MPMD, we have simulated a smaller hybrid nanostructure consisting of an oligothiophene (nT) (a n-thiophene rings oligomer, with n = 2,4,6) as electron donor and a ZnO cluster of 120 atoms as electron acceptor. Oligothiophenes are considered a good model for studying the electronic properties of P3HT, since the presence of hexyl chains in P3HT has mainly an effect on the solubility of the polymer, and it is not expected to alter its energy levels[124]. Regarding the ZnO cluster, we have chosen a hexagonal wurtzite zero-dimensional rod-like structure[125], which is a reduced-size model of the bigger one-dimensional nanoneedles studied in Chapter 2 and used in photovoltaics applications[126]. Furthermore, clusters of this specific size have been produced by laser ablation[127] and proven to be

particularly stable. A hierarchical combination of MPMD and DFT is adopded, providing a numerically efficient computational protocol to identify the minimum energy configurations of the hybrids. In this Chapter, we apply the ΔSCF scheme to study the energy-level alignment of the hybrid interfaces considered. From the methodological standpoint, a simple model is proposed for studying hybrid interfaces that only requires the ΔSCF calculation on their isolated components. For the specific case of ZnO-sexithiophene (6T), it is found that the interface is less favorable for charge separation at variance with the case of planar ZnO surface[108].

Most of this Chapter has been taken from *C. Caddeo et al., J. Phys. Chem. C 116 (2012)* (Ref. 128)

3.2 SYSTEM DESCRIPTION

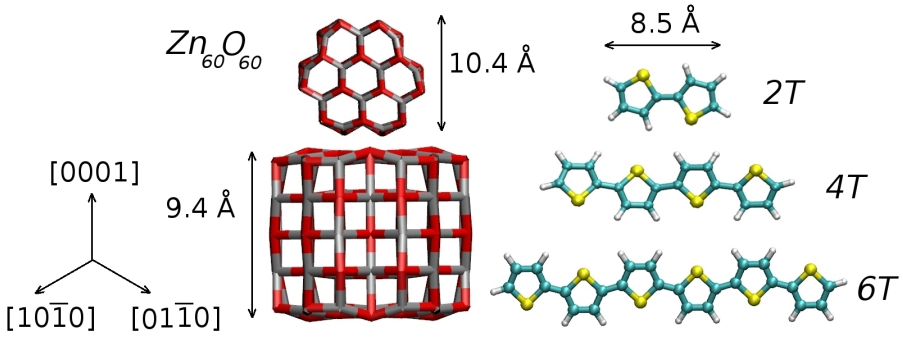

Figure 14: Left: top and side view of the $Zn_{60}O_{60}$ nanocluster. Right: View of the planar oligomers. In all figures, red is Oxygen, grey is Zinc, cyan is Carbon, yellow is Sulphur and white is Hydrogen.

In order to generate models of hybrid nanosystems, MPMD simulations were performed, combined with DFT calculations through the following multi-step procedure. At first the different building blocks of the hybrid systems (ZnO and nT) were considered separately, and their structures were fully relaxed at DFT level. The considered ZnO cluster has hexagonal cross-section along the [0001] direction, and exhibits six (10$\bar{1}$0) nonpolar facets. It has been obtained by cutting and relaxing a portion of bulk ZnO. It is represented in Fig. 14 together with the relaxed nT molecules. Three hybrid systems (hereafter labeled as HYB_2, HYB_4, and HYB_6) are then obtained by merging the ZnO

cluster and bithiophene (2T), quarterthiophene (4T) and 6T separately. Their structures are first relaxed using MPMD keeping the positions of all the ZnO atoms fixed at the DFT geometry, while the polymer is let free to move and relax following long range electrostatic and Van der Waals forces. It is known that the thiophene derivatives adhesion on the ZnO $(10\bar{1}0)$ surface is anisotropic, and it has been thoroughly described in Chapter 2. Thus, here the two preferred orientations of the oligomer were chosen as starting configurations and then a 100ps-long MPMD simulation at low temperature was performed, followed by a conjugate-gradient optimization. The same minimum was found for both the configurations, showing that the initial guess does not influence the final result. Finally, the MPMD resulting structures are fully relaxed at DFT level. In each SCF cycle, the energy was required to be converged within $3 \cdot 10^{-6}$ eV.

Quasiparticle energies are computed directly as total-energy differences in the framework of the ΔSCF scheme[109]. Since all the electronic excitations considered here are easily described in terms of isolated single-particle transitions, the application of the ΔSCF method is fully justified (see e.g. Ref.[129]). In particular, for an N-electrons system, any empty (occupied) level is corrected by calculating the total energy E_{N-1} (E_{N+1}) of the same system with an additional (missing) electron in it. Specifically, an empty (occupied) level is corrected by replacing its corresponding DFT eigenvalue with E_{N+1}-E_N (E_N-E_{N-1}). The accuracy of the method employed is confirmed by the computed ionization energy and electron affinity of the diatomic ZnO molecule, 9.40, and 2.21 eV respectively[125], in good agreement with the corresponding experimental values of 9.34±0.02[130] and 2.09±0.01[131] eV. Good agreement is also found for other properties calculated for the diatomic ZnO molecule, such as binding energy, vibrational frequency and bond length (see Table 2). Further computational details are provided in the Appendix section (Chapter A).

3.3 RESULTS AND DISCUSSION

3.3.1 *Morphology and energetics*

At first, a PBE/TZVP optimization of $Zn_{60}O_{60}$, 2T, 4T, and 6T separately was performed. During the geometry optimization of $Zn_{60}O_{60}$, the Zn-O double layers merge into single layers containing both Zn and O atoms. This phenomenon has been

	this work	CC[a]	PBE/DSPP/DND[b]	Exp
r_b	1.71	1.72	1.73	-
E_B	1.78	1.63	2.12	1.61±0.04[c]
ω_v	742	727.2	665	805±40[d]
EA	2.21	2.03	-	2.09±0.1[d]
IE	9.40	-	-	9.34[d]

[a] From Ref. 132

[b] From Refs. 133,134

[c] From Ref. 130

[d] From Ref. 131

Table 2: Comparison between calculated and experimental properties of the diatomic ZnO molecule. Bond lenghts (r_b) are in Å, energies (binding energy E_B, electron affinity EA and ionization energy IE) in eV and vibrational frequencies (ω_v) in cm^{-1}.

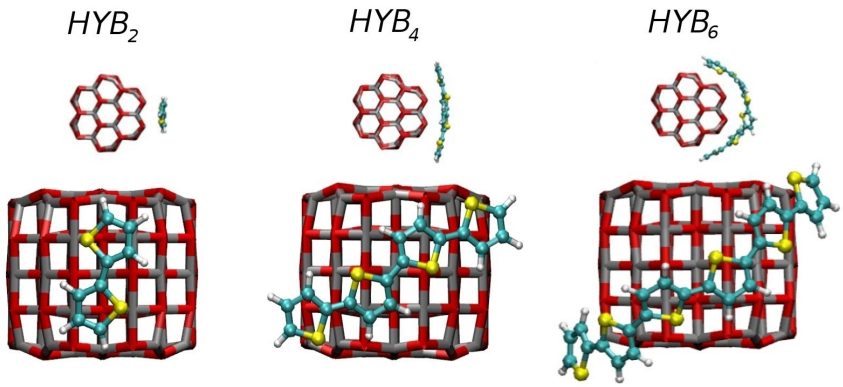

Figure 15: Top and side view of the three hybrids after the overall MPMD+DFT relaxing procedure.

observed before[135] and it is due to the presence of polar O-terminated and Zn-terminated surfaces which give rise to an electric field in the cluster[136]. Thus, the Zn and O ions with opposite charges move towards a common plane to find a relative stable state. This modification affects only the planes perpendicular to c axis, while the hexagonal cross-section is preserved. Starting from the separate optimized geometries the combined MPMD+DFT minimization procedure described in Sec. 3.2 was applied. The final optimized geometries of the three hybrids

considered are shown in Fig. 15. The optimal position of the nT with respect to the nanocluster is different from what obtained for P3HT on a flat $(10\bar{1}0)$ ZnO surface (see Chapter 2). In particular, the angle formed between the nT backbone and the [0001] direction of the nanocrystal increases at increasing nT length. This is a size effect: the organic molecules bend in order to maximize the interaction with the nanocrystal, while this distortion is not needed in the case of a flat surface.

The minimum energy structures in Fig. 15 do not differ significantly from their classical counterparts with the exception of HYB_6. In this case, in the final MPMD configuration the 6T does not wrap around the nanocrystal. This can be attributed to a too large stiffness of the molecule as described by the MP. After relaxing the hybrid structures, the adhesion energy U_{adh} of the nT on the ZnO nanocluster was calculated, defined as

$$U_{adh} = U_{hyb} - U_{ZnO} - U_{nT}, \tag{7}$$

where U_{hyb}, U_{ZnO}, U_{nT} are the total energies of the hybrid system, the optimized ZnO nanocluster, and the straight optimized nT, respectively.

The computed U_{adh} and the stacking distance d_{stack} between the center of the molecule and the nanocluster facet are reported in Table 3 (total). In order to separately account for dispersive and covalent contributions to the adhesion energy, all the calculation were performed again neglecting the dispersive forces. The results are reported in Table 3 as non-dispersive case. The effect of dispersive interactions on the geometries is to bend the organic molecule so as to adapt to the local curvature of the nanocrystal. This effect is larger for the longest molecules (4T and especially 6T), while it is negligible for the HYB_2 system. The structures obtained by neglecting the dispersive interactions are shown in Fig. 16.

Since no chemical bond is formed between the organic molecule and the nanocluster, it is correct to conclude that the adhesion is mainly given by dispersive forces. The total adhesion energy per monomer U_{adh}/mon is smaller than the experimental value of ~ 0.65 - 0.87 eV for thiophene on a flat ZnO surface[137]. This is expected given several adhesion reduction effects such as polymer strain, anisotropy and edges as described in Chapter 2. It is also worth noting that the nT adhesion increases with n. At variance, when dispersion is not included the adhesion converges to a constant value of about 0.3 eV. In this case the molecule does not wrap the nanocrystal and the

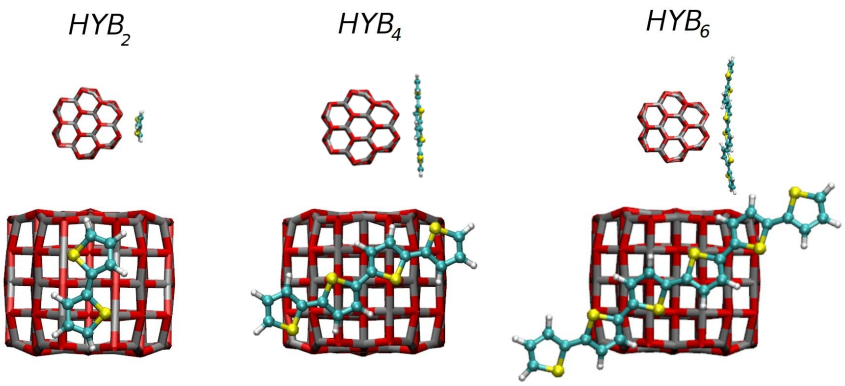

Figure 16: Top and side view of the three hybrids after the overall relaxing procedure. These geometries were obtained without taking into account the dispersive contributions.

	total			non-dispersive		
	U_{adh}	U_{adh}/mon	d_{stack}	U_{adh}	U_{adh}/mon	d_{stack}
HYB_2	1.31	0.65	2.7-2.9	0.45	0.22	2.8-3.2
HYB_4	1.34	0.34	2.4-2.9	0.29	0.07	2.6-3.1
HYB_6	1.96	0.33	2.8-3.0	0.29	0.05	2.9-3.3

Table 3: Adsorption energies (values in eV) and stacking distances (values in Å).

adhesion is only due to the two central thiophene rings. The adhesion energy in this case agrees with the results reported in Ref.[108] for 6T on ZnO surface calculated without dispersion. As for the stacking distance, it is found approximately constant for all nT lengths. A longer distance is found when dispersive interactions are neglected. The calculated values are again consistent with the ones described in Chapter 2 and are typical of a physisorption mechanism.

3.3.2 *Electronic properties*

In order to study the energy-level alignment at the interface, four levels must be considered, i.e. the HOMO and LUMO of the two components in the hybrid. These levels can be identified by examining both spatial distribution and energies of the molecular orbitals of the hybrid. For example, for the HYB_6 system, the LUMO and LUMO+1 levels of the hybrid corre-

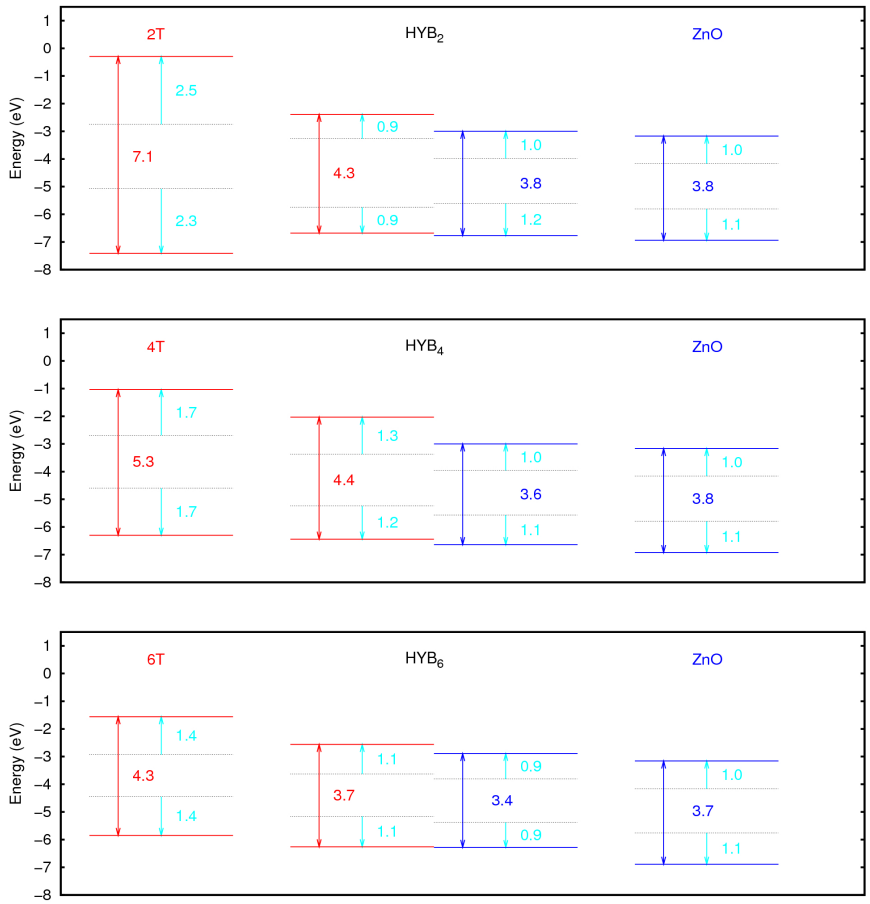

Figure 17: Energy-level alignment of the three hybrids considered as obtained with the ΔSCF method; dashed lines correspond to the DFT levels.

spond to the LUMO levels of the ZnO nanoparticle and of the 6T, respectively, while the HOMO and HOMO-1 levels of the hybrid correspond to the HOMO of the 6T and ZnO nanoparticle, respectively. The ΔSCF corrected levels are shown in Fig. 17 (middle). The levels of the separate components at the hybrid geometry are reported as well (left nT, right ZnO).

The interaction between the ZnO nanocluster and the nT molecule shifts the electronic levels of the separated components, with larger shifts for the nTs ($0.4 - 0.7$ eV) as compared to $Zn_{60}O_{60}$ ($0.2 - 0.4$ eV). These shifts can be attributed to an electronic coupling between the two components which induces a charge displacement from the nT to the metaloxide. This effect has been also observed for other organic molecules adsorbed onto inorganic surfaces[138]. In Fig. 18 the difference between

the electronic density of the interacting and non-interacting system is plotted. More specifically, the electronic densities of 2T, 4T, 6T, and $Zn_{60}O_{60}$ at the geometry of the interacting configuration have been subtracted from the electronic density of the hybrid systems. Fig. 18 shows that some charge is displaced from regions around the thiophene rings (green isosurfaces) to the region between the nT and the nanocrystal (orange isosurfaces). There is more charge displaced for HYB_2 and HYB_6 than for HYB_4, and this is reflected in the more pronounced levels shift observed for these systems (see Fig. 17). This effect is attributed to the lower adhesion of the terminal rings of the 4T chain to the nanocrystal. In fact, this molecule is too long to accommodate entirely on the $Zn_{60}O_{60}$ without bending its backbone (as the 2T), but too short to be flexible enough to wrap around the nanocluster as the 6T (see Fig. 18).

Fig. 17 shows that, for all the three hybrid systems studied, the energy-level alignment is unfavorable for holes transfer, as the HOMOs of the two moieties are almost coincident in all cases. The results for HYB_6 can be compared with those obtained in Ref.[108] for the same 6T on a $(10\bar{1}0)$ ZnO planar surface, in which the alignment of type-II is preserved. The reduced offset observed for HYB_6 is a consequence of the low dimensional nature of ZnO and the curvature of the molecule, that induce a different electronic coupling between the metaloxide and the organic molecule. This coupling shifts the original electronic levels of the separate moieties producing an alignment which is detrimental for holes transfer, since holes of the thiophenes are not prevented from being taken by the ZnO itself. In a realistic solar cell, however, the nanoclusters are typically embedded in a oligothiophene matrix, and different configurations can be expected due to the interactions between oligothiophenes. Thus, deviations from these results are possible.

3.3.3 *Predictive model for the QP alignment*

Provided that the hybridization between the two systems is not too strong, the quasiparticle corrections in the hybrid (Δ_i) can be approximated using a simple model. Indeed, each state i can be associated to one of the components taken separately. And, assuming that the screening is inversely proportional to the gap, one can write that:

$$(\Delta_i^{sep}/gap_{KS}^{sep}) \simeq (\Delta_i/gap_{KS})$$

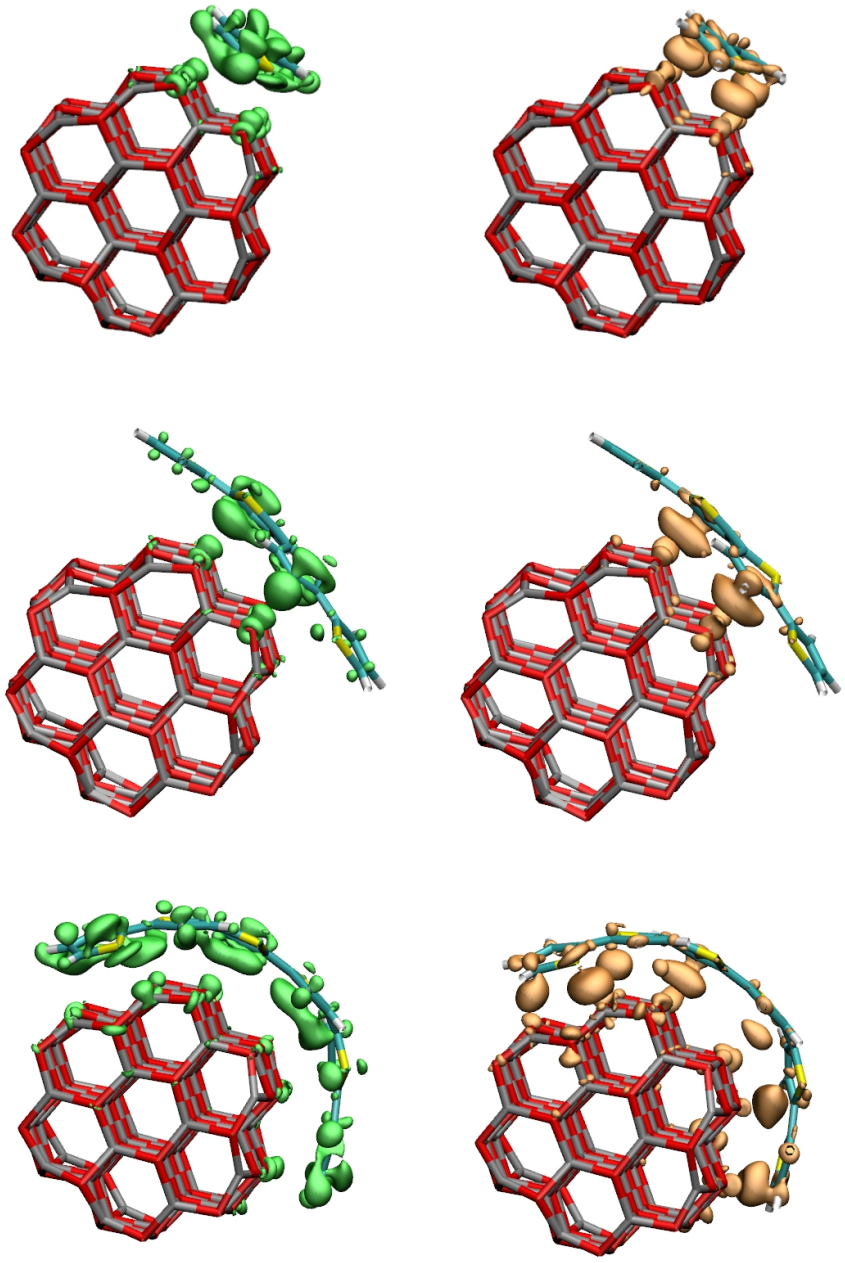

Figure 18: Difference density plots showing the displacements of electronic charge induced by the ZnO-nT interaction. Green isosurfaces (left panels) correspond to regions where the difference is negative, orange isosurfaces (right panels) where it is positive, showing that charge density moves from green regions to orange regions (isovalue equal to 0.001 e/a.u.).

		HYB_2		HYB_4		HYB_6	
		model	ΔSCF	model	ΔSCF	model	ΔSCF
nT	HOMO	-7.1	-6.68	-6.4	-6.44	-6.3	-6.26
	LUMO	-1.9	-2.39	-2.3	-2.03	-2.5	-2.56
$Zn_{60}O_{60}$	HOMO	-6.7	-6.77	-6.5	-6.64	-6.3	-6.28
	LUMO	-3.0	-3.00	-3.2	-3.00	-3.0	-2.89
gap		4.0	3.68	3.2	3.44	3.4	3.37

Table 4: Comparison between the QP levels as obtained via ΔSCF and the model described by Eq. 8.

where Δ_i^{sep} is the QP correction for the component associated to the i^{th} state taken separately, and gap_{KS} and gap_{KS}^{sep} are the Kohn-Sham gaps calculated in the hybrid and in the separate systems, respectively. As a result, the quasiparticle energies of the hybrid can be simply written as:

$$E_{i,QP} = \epsilon_{i,KS} + \Delta_i = \epsilon_{i,KS} + \left(\frac{gap_{KS}}{gap_{KS}^{sep}}\right)\Delta_i^{sep} \tag{8}$$

As shown in Table 4 the results of the model are always qualitatively consistent with the full ΔSCF calculation, with a better agreement at increasing system size. It is worth remarking that the SCF calculations of the hybrids involving the removal/addition of an electron from/to a level other than HOMO/LUMO are difficult since they converge slowly. The advantage of this model is to allow to use the results for the isolated components to obtain the QP levels, avoiding 4 single-point calculations on each hybrid system.

3.4 CONCLUSIONS

We have presented a systematic theoretical study on hybrid systems composed by a $Zn_{60}O_{60}$ hexagonal wurtzite nanocrystal and a oligothiophene molecule (bithiophene, quaterthiophene, and sexithiophene). Ground-state structural relaxations combining model potential molecular dynamics and all-electrons density functional theory calculations have been performed. Starting from the DFT electronic structure, the energy-level alignment between the organic and inorganic moieties has been accurately evaluated by means of the ΔSCF method. All the

junctions have been found to be ineffective for charge separation at the interface, as a consequence of the nanostructurization of ZnO and the curvature of the molecule, which induce an electronic coupling between the organic and inorganic component. In particular, a comparison between the case of $Zn_{60}O_{60}$-6T with the previously reported study of 6T on a flat $(10\bar{1}0)$ ZnO surface has been presented. While a type-II junction was found in the latter case, this staggered energy-level alignment is lost when the ZnO is nanostructured. Though this effect might be reduced for larger clusters, it definitely gives a trend for systems in which quantum confinement effects are important. From the methodological standpoint, a simple practical model which only requires to apply the ΔSCF method to the individual components of the hybrids has been proposed. This model provides results consistent with those obtained via the full ΔSCF for the composite systems.

Another system which would be interesting to study is a similar hybrid in which the electron acceptor is modeled as a ZnO rod-like one dimensional nanoparticle instead of a zero dimensional cluster. Since we calculate the electron affinities and ionization energies through the ΔSCF method, in order to apply our methodology to such a system one could for example build longer models of the hexagonal nanocluster, until the asymptotic limit of IE and EA for infinite rod is found. The latter could be calculated with different methods which are suitable for periodic systems, such as for example GW or other beyond-DFT methods.

In conclusion, though the use of nanoparticles can be beneficial to have blends with large interface area, we must stress that it may also have important drawbacks since the nanocurvature of the interface can negatively impact on the electronic levels alignment.

4

OPTOELECTRONIC PROPERTIES OF $(ZNO)_{60}$ NANOCLUSTERS

Contents

4.1 INTRODUCTION

In the previous Chapter we have studied the energy-level alignment of an hybrid system in which the electron acceptor was represented by a 120-atoms rod-like ZnO nanocluster. Though the results of Chapter 3 are not strongly dependent on the specific atomic configuration of the nanocluster, the latter is however important from a technological point of view: ZnO clusters of 120 atoms have in fact been produced and proven to be particularly stable and abundant[127]. Since these $(ZnO)_{60}$ clusters have a high atomic precision, they are of potential interest for future applications in nanoelectronics. They could be employed as building blocks in a bottom-up approach to design innovative nanostructured materials: for example they could be arranged in high-surface networks for bulk heterojunctions with applications in photovoltaics, photocatalisys or sensing[139–141]. However, the precise structure of the $(ZnO)_{60}$ is still unknown. The isomer identification at the atomic scale is an important challenge that has stimulated some theoretical research based on atomistic modeling[142,143]. Since the relative stability inferred from total energy calculations suffers from a strong dependence on the computational scheme adopted, we have combined it with optical spectroscopy to identify the most abundant geometrical structure of this cluster. This is the subject of the present Chapter, in which the results of a time-dependent DFT (TDDFT) study of the optoelectronic properties of a set of $(ZnO)_{60}$ isomers are presented. In this

study the ionization energies and the electron affinities were calculated as total energy differences between charged and neutral systems as described in Chapter 3. The optical absorption spectra are computed through a hybrid TDDFT scheme which has shown to accurately reproduce the experimental optical features of ZnO nanoparticles[144]. A similar approach has been adopted in literature to study the optical absorption and emission properties of $(ZnS)_4$ and $(ZnS)_6$ nanoclusters both in absence and in presence of water[145,146]. The obtained results show that the spectroscopic properties are markedly different for each structure, and suggest a way to distinguish between isomers by using the calculated absorption spectra as a fingerprint in comparison with experimental results.

Most of this Chapter has been taken from *C. Caddeo et al., Phys. Chem. Chem. Phys 14 (2012)* (Ref. 147).

4.2 SYSTEM DESCRIPTION

For small $(ZnO)_n$ clusters ($n \leqslant 32$) the generation of different isomers has been carried out in past literature by using genetic algorithms and performing a global minima search (see e.g. Ref. 148). This approach, however, is very difficult when dealing with a large number of atoms[133,149]. Therefore the different $(ZnO)_{60}$ isomers were built by following the descriptions in Refs. 133,149. In particular, the starting hexagonal prism structure (HEX) was obtained by cutting a cluster from the bulk WZ ZnO. The structures were then pre-optimized by means of MPMD simulations[45]. The MPMD resulting structures are then fully relaxed at DFT level, and their optical absorption spectra are obtained through TDDFT calculations. In each SCF cycle, the energy was required to be converged within $3 \cdot 10^{-6}$ eV. The use of MPMD as pre-optimizing tool allows us to save computational time, since the parameters used[150] have shown to provide ZnO cluster structures very close to the DFT optimized geometries (see also Chapter 3). Ionization energies (IE) and electron affinities (EA) are computed as total energy differences as in Chapter 3.

Further computational details are provided in the Appendix section (Chapter A).

4.3 RESULTS AND DISCUSSION

4.3.1 *Morphology and energetics*

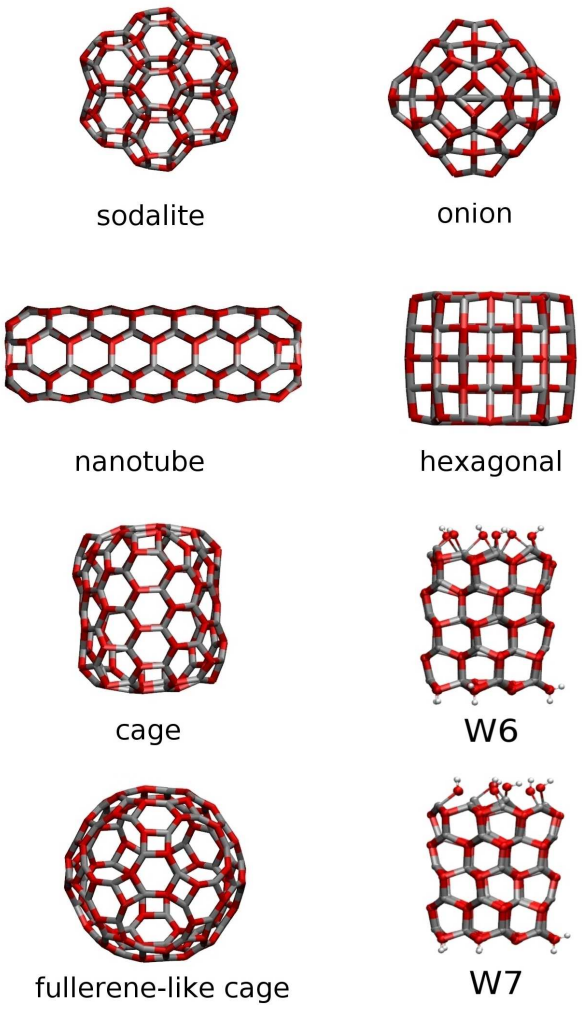

Figure 19: Optimized structures of the six unsaturated $(ZnO)_{60}$ clusters considered and of the two saturated models of the hexagonal cluster (W6 and W7).

The optimized geometries of the considered structures are shown in Fig.19. For the hexagonal isomer we observe the same modification of the bond lengths and angles described in Chapter 3. Also two saturated models of the hexagonal isomer have been considered, obtained by dissociating 6 and 7 water molecules on the polar surfaces before relaxation[144] (hereafter

referred to as W6 and W7). Consistently with previous results, these models preserve the WZ structure. Their geometries are reported in the bottom right part of Fig.19. The other five possible isomers of $(ZnO)_{60}$ considered are the nanotube, the cage and the fullerene-like cage, in which all atoms belong to the surface, and the sodalite and onion structures, which are half way between the all-surface structures and the bulk-like hexagonal. All these isomers are described more in detail in Ref. 133. In Table 5 the cohesive energy E_c (in eV per Zn-O dimer) of all isomers is reported, defined as

$$E_c = \frac{E_{tot}}{N} - (E_{Zn} + E_O) \tag{9}$$

where E_{tot} is the total energy of the isomer, N its number of Zn-O dimers, and E_{Zn} (E_O) is the energy of an isolated Zn (O) atom in its ground state. E_c is a measure of the relative stability of the system: higher values correspond to less stable clusters. The calculated values (all close to -6.4 eV/dimer) are larger than the bulk cohesive energy of ZnO (-7.5 eV/dimer)[125], as expected due to surface energy costs.

In Table 5 (second column) the DFT total energy differences ΔE with respect to the most stable isomer are reported as well: the sodalite turns out to be the lowest-energy structure, with the hexagonal nanocluster just 0.45 eV higher in energy. These results agree with that in Ref.[133] concerning the sodalite, but the energy ordering of the other isomers is different: for example, they find that the second lowest-energy structure is the cage, with a difference as large as 1.56 eV with respect to the sodalite. Such differences can be attributed to (i) the different XC functional used (BP86 here, Perdew-Burke-Ernzerhof[151] in Ref. 133); (ii) the methods chosen to represent the molecular orbitals: (all-electrons TZVP basis set here, double numerical with d-polarization functions plus pseudopotentials in Ref. 133). All in all, the above discussion implies that the identification of the most stable structure cannot be based entirely on total energy differences and should be better based on spectroscopic observables.

4.3.2 *Optoelectronic properties*

In columns four and five of Table 5 the ionization energies (IE) and electron affinities (EA) are reported. While the ionization energies are very similar for all isomers (~7.0-7.2 eV), the elec-

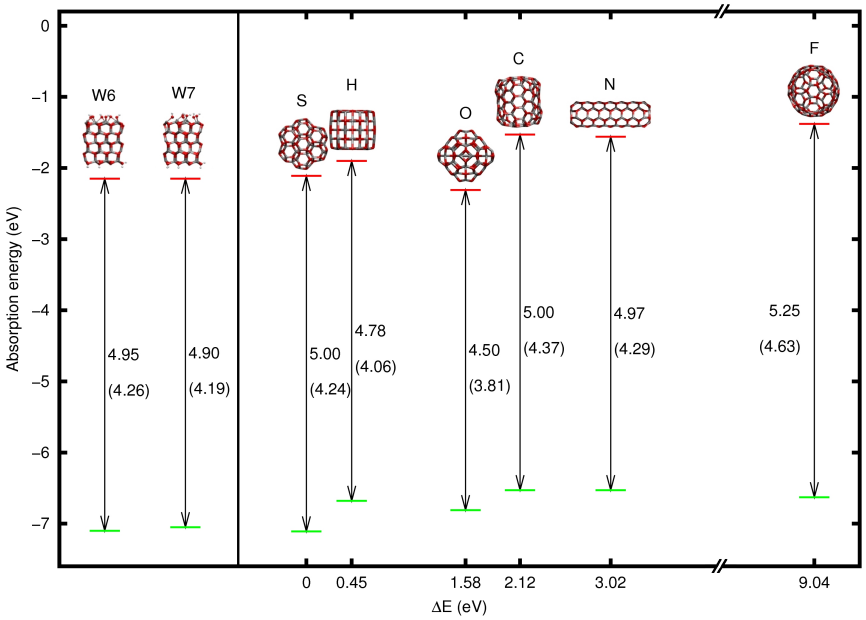

Figure 20: HOMO and LUMO levels as obtained with the modified B3LYP functional. The values in parenthesis correspond to the TDDFT optical gap. Capital letters on top refer to different isomers as follows: S=sodalite, H=hexagonal, O=onion, C=cage, N=nanotube, F=fullerene-like cage. The horizontal axis reports the differences in total energy (ΔE) with respect to the lowest-energy isomer (sodalite). On the left, the HOMO and LUMO levels of the two saturated clusters (W6 and W7) are reported out of the total energy scale.

tron affinities vary in a broader range (~2.9-3.6 eV). It is interesting to note that such large electron affinities are comparable with that of C_{60}, which is one of the most efficient electron acceptors used in organic electronics. In particular, by using the same theoretical framework (BP86/TZVP) for C_{60}, values of 7.44 and 2.75 eV are obtained for ionization energy and electron affinity, respectively, in good agreement with the experimental values of 7.6 and 2.7 eV[152].

Starting from the optimized geometries, a single-point energy calculation with the B3LYP functional has been performed to obtain the Kohn-Sham eigenvalues. The corresponding energy-level diagram is shown in Fig.20. The energies and spatial distribution of the highest occupied (HOMO) and lowest unoccupied molecular orbitals (LUMO) are reported in Figs.21 and 22. All the orbitals in Fig.21 have a symmetric spatial distribution, with the exception of the HOMO of the hexagonal isomer. This asymmetry is due to a level degeneracy: the HOMO-1 level, in

isomer	ΔE_{TZVP}	E_c	IE	EA
sodalite	0	-6.47	7.20	3.23
hexagonal	+0.45	-6.46	7.16	3.25
onion	+1.58	-6.44	7.04	3.57
cage	+2.12	-6.43	7.09	3.11
nanotube	+3.02	-6.42	7.03	3.15
fullerene	+9.04	-6.32	7.20	2.91

Table 5: Differences in total energies with respect to the lowest-energy isomer (first column); cohesive energies (second column); ionization energy and electron affinity (last two columns). All values are in eV.

fact, has the same energy of the HOMO and it is spatially distributed in a mirror-like way with respect to the HOMO.

A common feature of all the considered structures is the delocalized nature of the LUMO level, which has been found also for other ZnO nanostructures[144,153], for C_{60} [154,155] and for the C_{60}-derivative PCBM[156].

It is interesting to notice that all the clusters have a well-opened band gap and do not present intra-band gap states. In particular, for the HEX isomer, the HOMO and LUMO levels are only slightly upshifted with respect to the water-saturated W6 and W7 clusters. Furthermore, the two saturated models exhibit practically the same energy levels, thus we consider them as equivalent. Similar results have been found previously for other water-saturated ZnO clusters[153]. A more detailed energy-level diagram is reported in Fig. 23.

The electronic structure of the considered nanoclusters is further analyzed in terms of density of states (DOS). In Fig.24 the DOS of the hexagonal isomer is reported as an example (solid line). The DOS of all the other isomers have similar features. In particular there are always four peaks in the valence band, already discussed in the literature[153,157] and referred to as P_I, P_{II}, P_{III} and d. The first peak in the valence band (P_I) is due to the valence *p* electrons of O atoms, while the P_{II} and d peaks arise from the 4*s* and 3*d* electrons of Zn atoms, respectively. The P_{III} peak is related to the *s* electrons of O atoms. The distance between the d peak and the valence band maximum is in agreement with experimental data[157]. For comparison, the DOS of the W7 cluster is also reported in Fig.24 (dashed). Con-

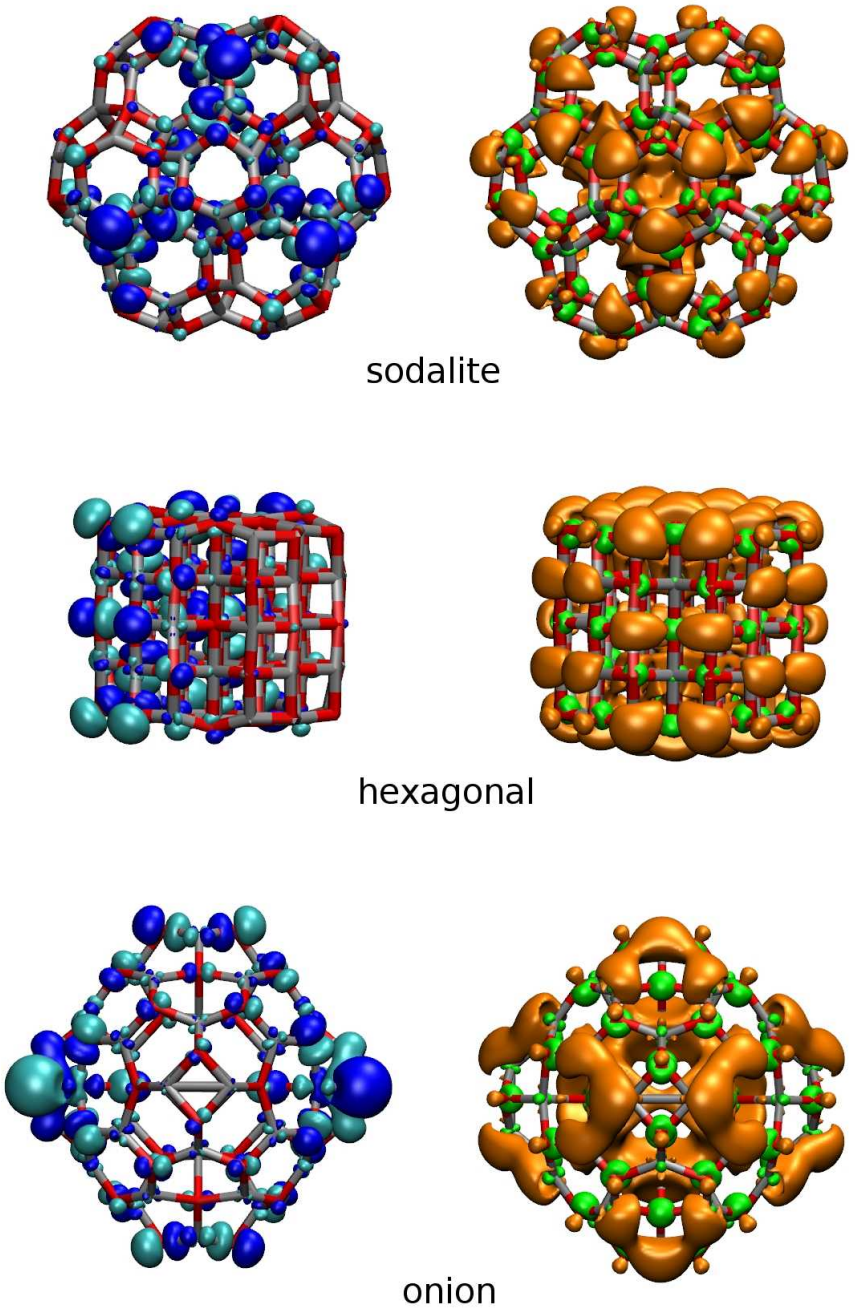

Figure 21: Orbital spatial localization (HOMO left, LUMO right) of the sodalite, hexagonal and onion isomers.

sistently with the results on the frontier orbitals, the two saturated nanocrystals exhibit almost indistinguishable DOS patterns and they are very similar to those obtained in Ref.[153] for bigger water-saturated ZnO clusters. Furthermore, their DOS

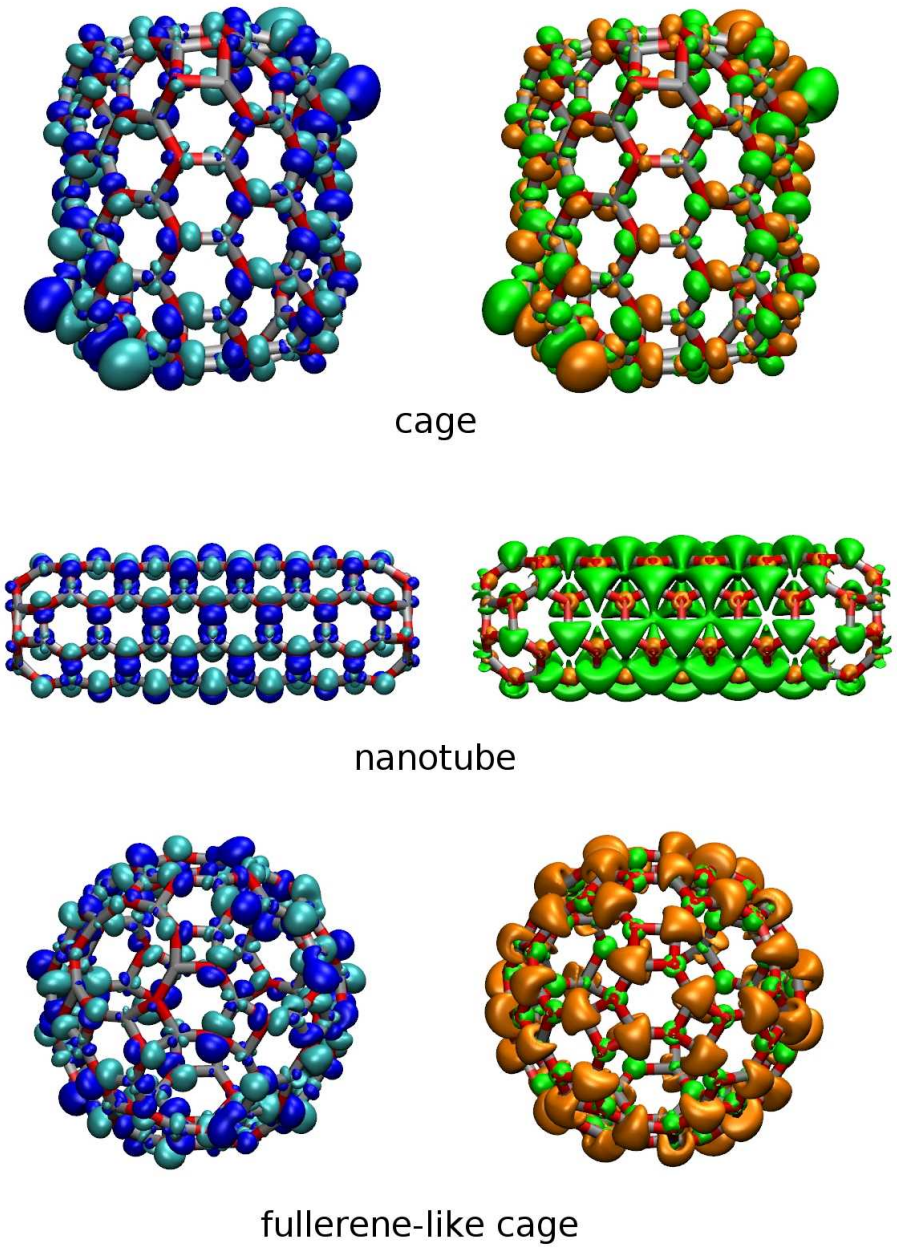

Figure 22: Orbital spatial localization (HOMO left, LUMO right) of the cage, nanotube and fullerene-like cage isomers.

is only slightly upshifted in energy with respect to that of the unsaturated HEX cluster.

TDDFT calculations are then performed to obtain the optical absorption properties. The computed optical gap (i.e. the first optically active electronic transition) is reported in Fig.20 within parentheses. A direct comparison of these data with experimental results is not possible since, as mentioned before, no

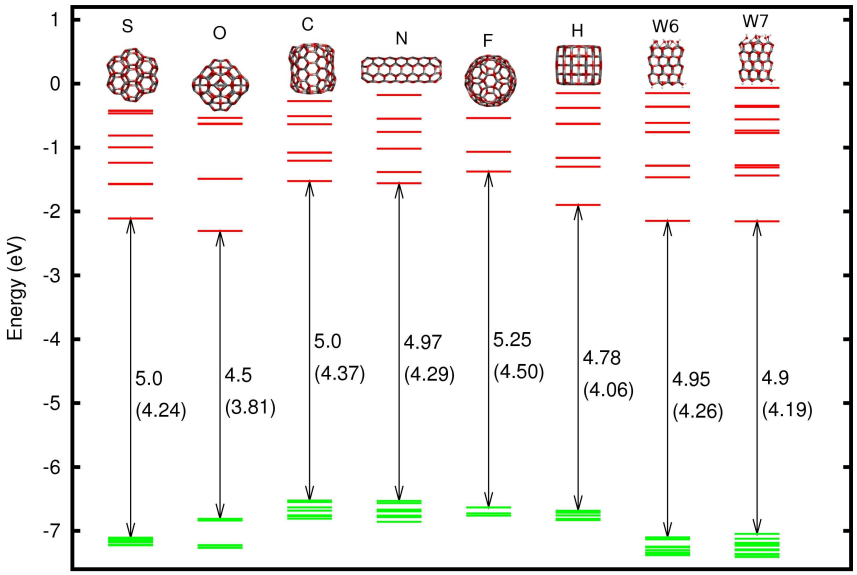

Figure 23: First ten occupied and unoccupied levels as obtained with the modified B3LYP functional. The values in parenthesis correspond to the TDDFT optical gap. Capital letters on top refer to different isomers as follows: S=sodalite, H=hexagonal, O=onion, C=cage, N=nanotube, F=fullerene-like cage, W6= hexagonal saturated with 6 water molecules, W7= hexagonal saturated with 7 water molecules.

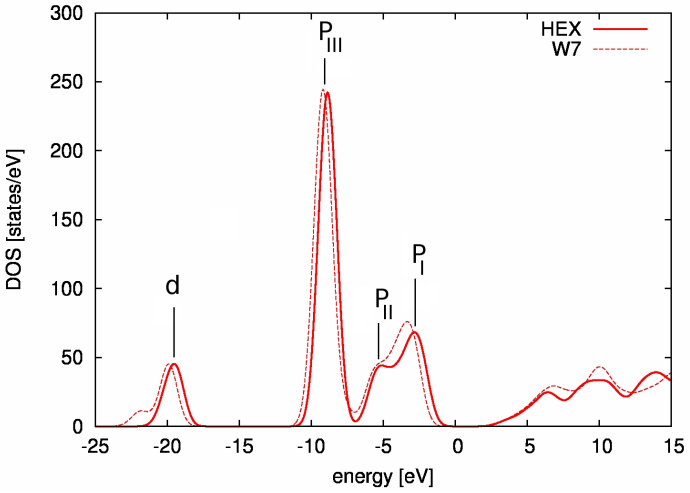

Figure 24: Density of states (DOS) of the hexagonal nanocluster, unsaturated (solid line) and saturated with 7 (dashed line) water molecules. The energy zero has been aligned to the Fermi energy.

experimental data are available on the electronic structure of $(ZnO)_{60}$ clusters. However, particles with radii below or equal to 0.3 nm have been reported to exhibit an absorption edge at ca. 4.0 eV[8]. From Fig.20 one can see that the isomers show different absorption onsets, which vary in a wide range from 3.81 to 4.63 eV.

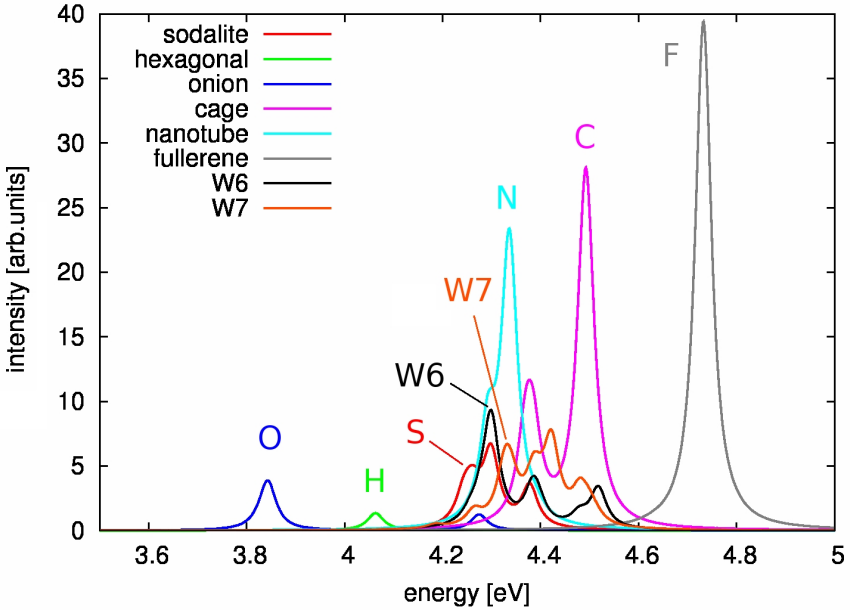

Figure 25: Optical absorption spectra of all the considered clusters.

Fig.25 shows the optical absorption spectra of all the considered structures. For all the isomers the first 10 optical transitions have been calculated, with the exception of the fullerene-like cage, for which a larger number of transition were necessary (the first 16 transitions are optically dark). A number of dark transitions are present also in the spectra of other isomers. For example, the three lowest-energy transitions for the cage are dark. The reasons of the presence of such dark states can be found in the symmetry of the structures. The highest the symmetry (fullerene-like cage), the more the number of prohibited transitions. This phenomenon has also been observed for carbon fullerenes with high symmetry (C_{60}). From Fig.25 it is apparent that saturation effects are important in the spectrum: a detailed comparison between the spectra of the saturated and unsaturated hexagonal clusters (up to ~4.5 eV) is reported in Fig. 26. Furthermore, at variance with the case of the unsaturated hexagonal cluster, the two saturaded clusters do not have dark states, as a consequence of the breaking of symmetry tue to the presence of the absorbed hydrogens and oxygens.

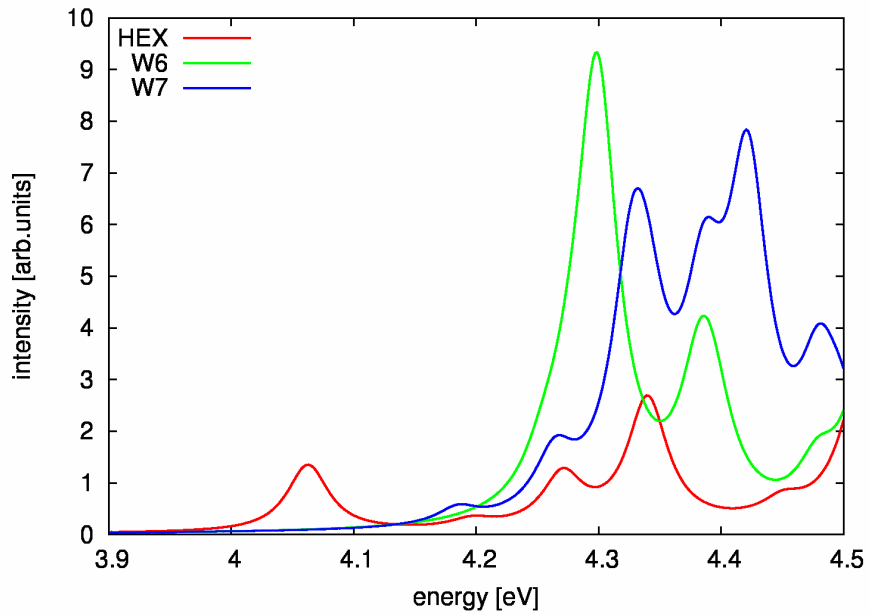

Figure 26: Comparison between the optical absorption spectra of the unsaturated hexagonal cluster and its two saturated counterparts.

Hereafter, the analysis will focus only on unsaturated clusters, ideally obtained in an impurity-free environment. All the clusters are transparent in the visible spectrum, with significant differences among the different isomers in the absorption onsets, all falling in the ultraviolet. In particular, the onion has the lowest energy absorption, being the only structure able to absorb below 4 eV. Between 4 and 4.2 eV, only the hexagonal cluster has optically active transitions. At quite higher energies, only the fullerene-like cage has its first absorption peak (at 4.63 eV). In the range 4.2-4.4 eV, three structures (sodalite, nanotube and cage) start absorbing. However, the sodalite and the cage absorption peaks are separated by 0.1 eV and could be distinguished. As for the nanotube, it can be identified because (i) its spectrum presents only one peak in that region, while there are two peaks for sodalite and onion, (ii) its intensity is about six times (two times) stronger than for sodalite (cage).

In Table 6 we report the energy of the lowest optically active transitions for all the isomers, together with the value of the corresponding oscillator strength and the type of transition. It is interesting to notice that only for the hexagonal case the transition is mainly a HOMO-LUMO transition, while for the other isomers other levels deeper than the HOMO are involved in the absorption.

isomer	E_t [eV]	f [arb. units]	T
sodalite	4.38	0.20	(H-11) $\rightarrow$ L
hexagonal	4.06	0.05	H $\rightarrow$ L
onion	3.84	0.09	(H-4) $\rightarrow$ L
cage	4.49	1.18	(H-6) $\rightarrow$ L
nanotube	4.34	1.39	(H-1) $\rightarrow$ L
fullerene	4.73	0.83	(H-28) $\rightarrow$ L

Table 6: Energies, strengths and nature of the lowest transitions with appreciable strength.

isomer	DFT B3LYP			TDDFT (SVP)	TDDFT (6-311G*)
	HOMO	LUMO	GAP	GAP	GAP
sodalite	-7.11	-2.11	5.00	4.24	4.30
hexagonal	-6.68	-1.90	4.79	4.06	4.09
onion	-6.81	-2.31	4.51	3.81	-
cage	-6.53	-1.53	5.00	4.37	-
nanotube	-6.53	-1.56	4.97	4.29	-
fullerene	-6.63	-1.38	5.26	4.50	-
W6	-7.10	-2.15	4.95	4.26	-
W7	-7.05	-2.15	4.89	4.19	-

Table 7: First three columns: HOMO, LUMO and HOMO-LUMO gap of the considered isomers. Last two columns: optical gap as computed by B3LYP TDDFT with SVP and 6-311G* basis sets, respectively. All values are in eV.

At variance with the total energy calculations the optoelectronic properties are less affected by the details of the theoretical framework. For example, calculating the energy levels and the spectra of the lowest energy isomers (sodalite and hexagonal) by using the combination B3LYP/6-311G* gives consistent results for the first optically active transitions. A comparison between the energy levels and the optical gap can be found in Table 7.

The absorption properties (both intensity and peaks position) can be combined with the results on the formation energy in order to better compare with experiments. In real experimental conditions, it can be assumed that different isomers are present at the same time, with a larger abundance for structures

with lower formation energy. Assuming thermal equilibrium at temperature T, the isomer population is expected to follow a Maxwell-Boltzmann distribution. The relative abundance (P_i) of an isomer i with respect to the population P_0 of the most stable one is

$$\frac{P_i}{P_0} = exp\left(\frac{-\Delta E}{k_B T}\right) \tag{10}$$

where $\Delta E = E_i - E_0$ is the corresponding energy difference between the two, and k_B is the Boltzmann constant. At temperatures such that $k_B T << E_i - E_0 = \Delta E$ the distribution is dominated by P_0 ($P_0 >> P_j$ for any j). At $k_B T \geqslant \Delta E = E_i - E_j$ the higher energy isomers appear. In the actual case $E_1 - E_0 = 0.45$ eV and at room temperature the absorption spectra is expected to be practically identical to that of the sodalite. A temperature of ~2300 K is required to have a 10% abundance of the HEX isomer and an absorption peak is expected to be detectable in the region 4.0-4.2 eV, where no other peaks are present. This analysis, being sensitive to the energy ordering, could be used also to validate different theoretical results. For example, according to Ref. 133, the cage and not the hexagonal is the second lowest-energy isomer, and $E_1 - E_0 = 1.56$ eV. A temperature as large as ~7800 K would be necessary to have a spectrum differing from that of the sodalite in the range 4.3-4.5 eV.

4.4 CONCLUSIONS

A systematic computational study of the energetic, electronic and optical properties of six $(ZnO)_{60}$ nanoclusters has been carried out, with the aim to provide a useful tool to identify its most abundant structure. Since the relative stability inferred from total energy calculations alone is strongly dependent on the computational scheme used, they have been combined with optical spectroscopy. The structures have been optimized via DFT calculations, using a basis set / XC functional combination which is accurate for ZnO clusters. The vertical ionization energies and electron affinities have been obtained by computing total energy differences between charged and uncharged systems. The electron affinities have been found to vary in a broad range and to be comparable (for all the clusters) with C_{60}, which is one of the most efficient electron acceptors used in organic electronics. This feature makes them all good candidates for use as electron acceptors in optoelectronic devices. TDDFT-B3LYP calculations have been performed to obtain the optical absorption

spectra of all the six structures. The calculated spectra are significantly different for different isomers and can thus be used in association with total energy data and in comparison with experiments to identify the ground state of $(ZnO)_{60}$.

The knowledge of the most abundand structure of the $(ZnO)_{60}$ allows on the one hand to further detail the energy-level alignment with the electron donor, and it paves the way to the possibility of using the nanoclusters as building blocks to obtain high precision bulk heterojunctions with improved photoconversion properties.

5

POLYMER WRAPPING ON CARBON NANOTUBES

Contents

5.1 INTRODUCTION

P3HT-SWNT systems are another class of nanostructured donor/acceptor complexes which are employed in third generation photovoltaics. Polymer-nanotubes blends are typically synthesized by dispersing the nanotubes into an aqueous solution containing the polymer[80,81], provided that the latter is soluble. The polymer coats the SWNT giving rise to a complex organization on the nanotube surface at the nanoscale. In some cases (e.g. for stiff short polymer chains[158]) the polymer aligns along the carbon nanostructures, but typically the polymer wraps around the nanotube giving rise to helical or pseudo-helical structures. At variance with the case of P3HT-ZnO systems, the polymer wrapping on carbon nanotubes has been experimentally observed[81,82,159]. However, despite of the considerable number of experimental investigations, the pseudo-helical structure observed for P3HT is still not understood. Furthermore, the stability of the wrapped configuration, once the solvent has been dried, must be identified. This is important from the technological point of view, since such blends operate in solvent-free environment and possible unwrapping phenomena can be present. Finally, understanding at the atomic-scale the stability of the wrapped configuration could aid the design of highly oriented P3HT-SWNT systems with improved conducting properties.

We have thus carried out an atomistic study of P3HT chains of realistic length wrapped on carbon nanotubes of different chiralities and at different temperatures. The system has been

studied via MPMD, which is a suitable computational tool to study large size systems for long simulation times. We provide evidence that, in absence of any solvent, the polymer tends to align along the nanotube. In addition, it is shown that the experimentally observed pseudo-helical organization[82] actually corresponds to a metastable configuration, whose lifetime depends on temperature and polymer length. The obtained results at finite temperature are in agreement with the pseudo-helical morphology characterized by Scanning Tunneling Microscopy[82], confirming the role of the nanotube chirality. Finally, a strong stabilization effect on the wrapped configuration due to neighboring polymer chains is demonstrated.

Most of this Chapter has been taken from *C. Caddeo et al., J. Phys. Chem. C 114 (2010)* (Ref. 160.)

5.2 SYSTEM DESCRIPTION

The simulation cells have dimensions L_x, L_y and L_z, along the x, y and z directions respectively, where $L_x = L_y = 5$ nm, and L_z ranged in the interval $0.013 - 0.1$ μm. The nanotubes were aligned along z direction and periodically repeated so as to represent an infinite structure. The simulated systems contained up to $2 \cdot 10^4$ atoms corresponding to a maximum polymer length $L \sim 0.1$ μm. All the computational details are described in the Appendix section (Chapter A).

5.3 RESULTS AND DISCUSSION

First the case of (15,0) zigzag nanotubes is considered. In order to have an initial configuration representative of the wrapped morphology (hereafter named HH) the polymer molecule was bent into an helical shape around the nanotube and the atomic forces were relaxed until a minimum energy configuration was identified. At variance with the approach used on P3HT-ZnO hybrids (see Chapter 2), here we fix the coiling angle and vary the temperature and polymer lenght. The actual value of the coiling angle (i.e. the angle formed by the polymer backbone with respect to the nanotube axis) is $\sim 30°$ and it was chosen according to experimental indications[82] and used for all the polymer chains investigated. After the relaxation procedure, the coiling angle in the HH configuration was found slightly changed, but

the periodicity of the helix was preserved (see top left panel of Fig. 27). The average polymer-nanotube distance was found to be as small as ~ 0.35 nm.

In order to study the wrapped morphology and the possible configurations at finite temperature, the HH systems were annealed for up to 4 ns in the range of temperatures $100K < T < 1000K$. The polymer length was varied in the interval $28L_P < L < 256L_P$, where L_P is the length of the monomer, a range of lengths comparable to the experimental data.

At any $T > 100$ K the polymers were found to move along the nanotube surface, thus exploring quite a few configurations differing by number of coils, coiling angles and morphologies; all structural features depend on both L and T. The possible configurations are reported in the top panels of Fig. 27. Interesting enough, no polymer desorption was observed in the thermodynamic conditions explored in the present investigation.

The different morphologies are distinguished by using the alignment parameter ξ, defined as

$$\xi = \frac{1}{N_U} \sum_{i=1}^{N_U-1} \frac{\vec{v_i} \cdot \vec{v_{i+1}}}{|\vec{v_i}| \cdot |\vec{v_{i+1}}|} = \frac{1}{N_U} \sum_{i=1}^{N_U-1} \cos(\theta_i) \qquad (11)$$

where the vector $\vec{v_i}$ connects the i-th and $(i+2)$-th equivalent sulfur atoms along the backbone, and N_U is the number of periodic units of the polymer ($N_U = L/2L_P$). According to Eq. 11, θ_i is the angle describing the bending of the polymer chain. ξ was found to vary in the range 0.6-1.0 depending on the different morphologies explored. In particular, a value $\xi \sim 0.8$ is found for the HH configurations, while the largest values ($\xi \sim 1$) are obtained when the polymer lies along the polymer axis and the neighboring polymer units are aligned. Finally, a small alignment parameter ($\xi \sim 0.6$) corresponds to the folded C phase.

In bottom panel of Fig. 27, the parameter $\xi(L, T)$ is calculated as a function of the annealing temperature and chain length. Colors identify the different polymer arrangements after annealing as long as 2 ns. The alignment parameter was evaluated on a regular mesh of $7 \times 6 = 42$ points, marked in Fig. 27 by triangular symbols, and then interpolated with a thin plate spline algorithm[161] to obtain the colormap in Fig. 27. A convergence test on the number of points was performed, and it was found that by increasing the mesh from 20 to 42 points the maps are practically unaffected. For a fixed polymer

length L, the above diagram shows that the ideal helical configuration (HH morphology) is stable only at very low temperature (blue region). At higher temperature the polymer relaxes into pseudo helical structures (H) similar to the experimentally observed ones[82]. By further increasing the temperature, the coils are spontaneously loosed during the dynamics and the polymer ends into the aligned morphology (A). For very high temperatures the polymer can even fold into a cloud configuration (C). According to the above analysis the H morphology

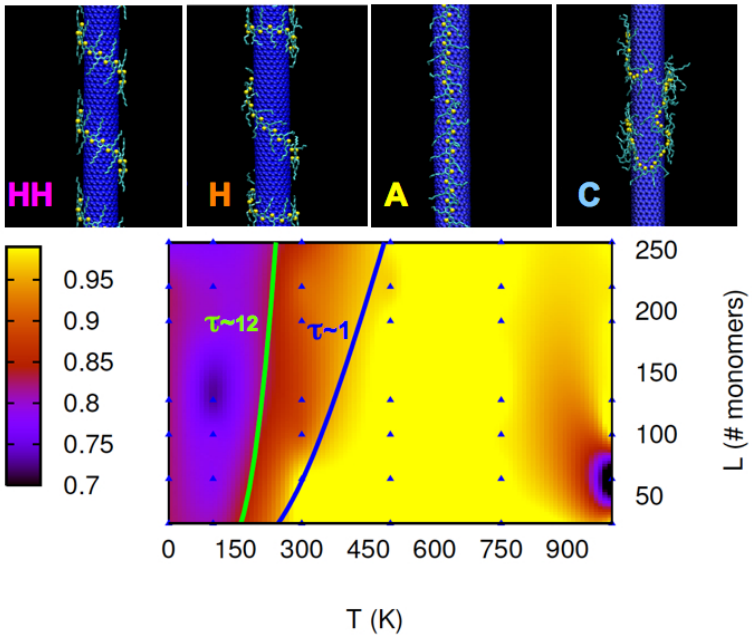

Figure 27: (Top panels) Identified ordered (HH, H, A) and folded (C) polymer configurations. (Bottom panel) Alignment parameter ξ as a function of temperature T and polymer length L. Lifetime curves (green and red lines) are identified by connecting points with identical helical lifetime (see text).

at room temperature is only a metastable configuration and it spontaneously changes into the aligned one.

In order to better characterize the lifetime of the H morphology and the physical factors affecting its stability, the instantaneous number of coils $g(t)$ of the polymer chain at time t was calculated:

$$g(t) = \frac{1}{2\pi}\sum_{i=1}^{N_U-1}\theta_i = \frac{1}{2\pi}\sum_{i=1}^{N_U-1}\arcsin\frac{\vec{v_i}\cdot\vec{v_{i+1}}}{|\vec{v_i}|\cdot|\vec{v_{i+1}}|} \qquad (12)$$

where θ_i, $\vec{v_i}$ and N_U have been defined above. At high temper-

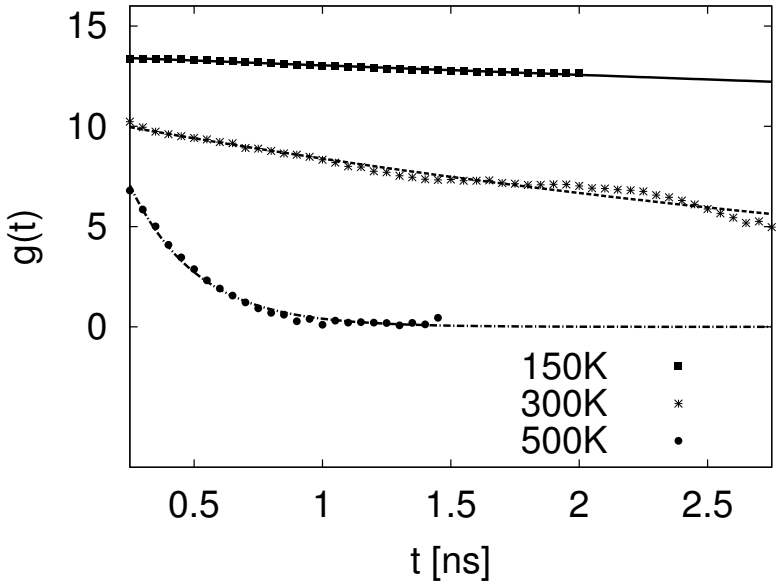

Figure 28: Number of coils as a function of the annealing time for a 256-monomer long chain at different temperatures

atures any molecule unwraps and, accordingly, $g(t)$ is found to monotonically decrease down to zero during the MPMD run. Conversely, at lower temperatures the unwrapping mechanism is less efficient and at the end of the simulations there is still a finite number of coils ($g(t) > 0$). The above picture for P3HT is in contrast with the spontaneous tendency of PPV to wrap at room temperature[162]. This can be attributed to the different chemical composition of the two polymers (e.g. the PPV does not contain sulfur atoms).

The atomistic data are well reproduced by an exponential function of time $g(t) \sim g(0)exp(-t/\tau)$ where τ , hereafter referred to as the lifetime of the wrapped H morphology, depends on both T and L, and $g(0)$ is the initial number of coils. A graph of the number of turns vs time is reported in Fig. 28. It shows the time evolution of the number of turns $g(t)$ for three different temperatures and the exponential functions used to fit data. The inverse of the lifetime $\sim 1/\tau$ corresponds to the rate of unwrapping events and it controls the kinetics. At early times in fact the rate of coils loss dg/dt is approximately $dg/dt \sim -1/\tau$. The lifetime τ decreases as the temperature increases according to an Arrhenius law $\tau \sim exp(E_a/kT)$, where E_a is the activation energy for an unwrapping event (see Fig. 29). E_a was calculated to be as small as 0.09 eV. According to the above analysis, the

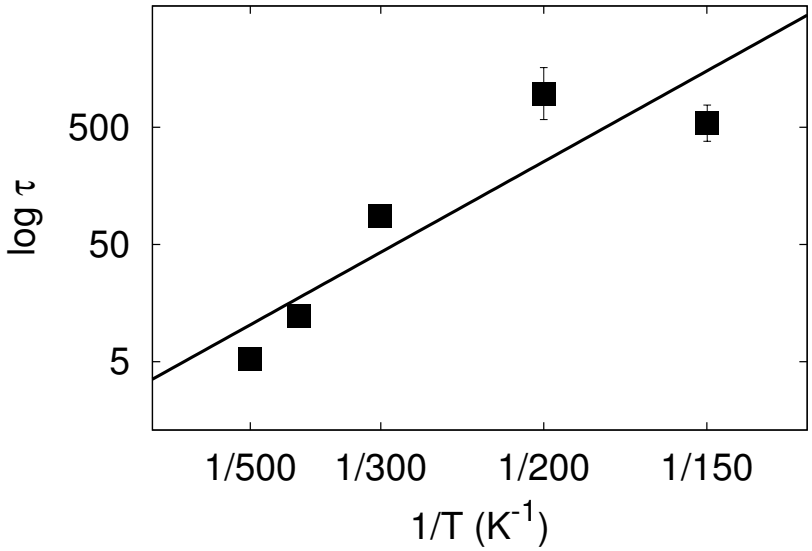

Figure 29: Unwrapping time versus temperature

HH morphology is stable and distinguished from the H one at very low temperatures, while, at higher temperatures, it can relax into H and eventually A configurations, by overcoming the energy barrier E_a.

Concerning the role of the polymer length L on the unwrapping kinetics, it is found a linear relationship $\tau \sim \kappa L$ with a lifetime per unit of length ($\kappa = \tau/L$) that is approximately independent on L. Accordingly, in the limit $L \to \infty$, the unwrapping kinetics is unchanged. This is shown in Fig. 30 and it suggests that the lifetime per unwrapping event is approximately constant, i.e. the unwrapping events are uncorrelated. This is accurately true in the early stages of the kinetics where $g(t)$ is linear, i.e. $g(t) \simeq -\frac{1}{\tau} \cdot t$. Possible deviations can be easily incorporated into the model by introducing an exponent α in such a way that $g(t) \sim L^{\alpha}$. The results of the above analysis can be summarized by introducing an overall $T - L$ dependence into the kinetic model for the wrapped morphology lifetime:

$$\tau(T, L) = \frac{L^{\alpha}}{\nu_0} e^{\frac{E_a}{kT}} \tag{13}$$

where ν_0 is a suitable constant. Here $\alpha = 1$ has been used. The above model correctly predicts that the lifetime of the wrapped H morphology is a continuous function of L and T, and it is longer for longer polymers and lower temperatures.

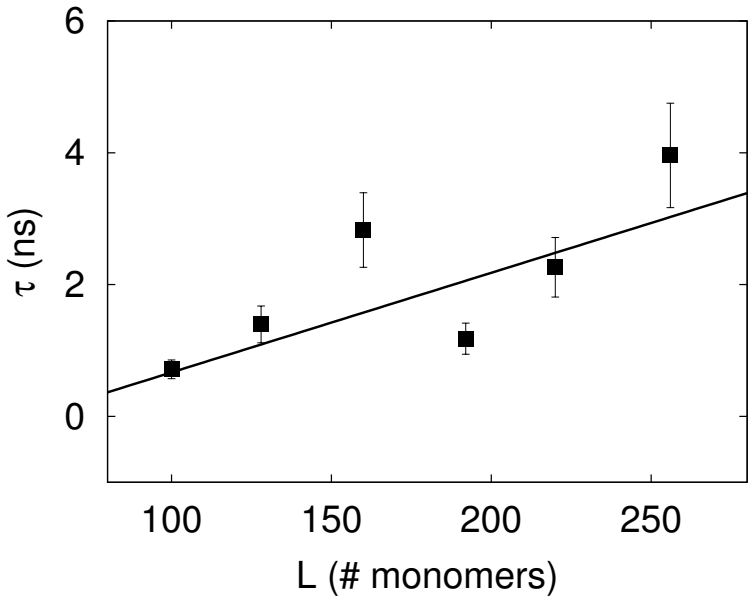

Figure 30: Unwrapping time versus polymer length

A remarkable result is that such a model is able to identify the boundaries in the L-T plane (Fig. 27) between the different morphologies. The points with the same lifetime τ_0 give rise to the curve $\tau(L, T) = const = \tau_0$. Different values of τ_0 correspond to different curves. It is possible to choose τ_0 in such a way that the corresponding curve approximately delimits the yellow region where the polymer is highly aligned ($\xi > 0.98$). This is obtained for $\tau_0 = 2$ ns. The corresponding curve is reported in Fig. 27 as a red line. Hereafter, all the lifetimes are normalized to $\tau_0 = 2$ ns. Accordingly, the points on the right of the red curve (i.e. $\tau < 1$) correspond to highly aligned polymers for which $\xi > 0.98$ (yellow shaded area); the points on the left (i.e. $\tau > 1$) have a smaller degree of alignment. The case of a larger lifetime ($\tau = 12$) is reported for comparison (green line). Three different polymer morphologies can be identified in the $L - T$ plane referred to as HH (regular helix when $\tau >> 1$), H (pseudo helix when $\tau > 1$) and A (aligned chains when $\tau \leqslant 1$).

At very high temperature, entropic contributions make possible a partial folding of the polymer and the model is not applicable. The folded phase (C) is recognizable in the ξ color map as the dark region at high temperature and length $\sim 60 L_P$.

A snapshot of a polymer wrapped in the H morphology on a (15,0) nanotube at T=300K is reported in Fig. 27. It exhibits clear similarities with the experimental structure of Ref.[82],

where different coiling angles alternate along the chain. Thus we suggest that the experimentally observed structure corresponds to a state that, in vacuo and at room temperature, is only metastable.

The theoretical results also demonstrate that the polymer morphology depends on the chirality of the nanotube, as indeed also suggested by experiments[82] and previous theoretical works[163]. In Fig. 31 the results for two systems differing only by the chirality of the nanotube are compared (the case of (15,0) zigzag and the case of a (9,9) armchair nanotube of similar radii). At T = 300K both systems unwrap during 2ns-long thermal annealing and we observe different morphologies during the run. The obtained morphologies differ qualitatively in terms of both the coiling angles and their relative abundance. In the zigzag case the polymer forms ~ 13 coils with angle ~ 60° and only two with angle ~ 30° while in the armchair case, there are ~ 4 coils with angle ~ 45° and ~ 8 coils with angle ~ 30°. This implies that the SWNT chirality has an important role on the final morphology of the system. In particular, the obtained results are in agreement with STM measurements on zigzag nanotubes[82]. The observed polymer configuration presents coils of angle $33° \pm 1°$, as found in the atomistic models (see Fig. 31, left). As for the predicted coiling angles in the armchair case, there is an agreement with some experiments[164]. Unfortunately, the comparison is difficult since in that work the chirality of the nanotubes has not been fully characterized. The actual values of the coiling angles are determined by the thiophene/nanotube lattice matching as shown in the insets of Fig. 31. An interesting feature of the wrapped conformations in both cases is the presence of clusters of two or more neighboring coils at the polymer extrema. This behavior is driven by the polymer-polymer interchain attractions and it corresponds to an ordered interdigitation of hexyl chains (see top left inset of Fig. 31).

So far systems with a single polymer chain per nanotube have been considered; however, real blends actually exhibit very high polymer density (1-0.1% wt nanotubes[82,165]) and several polymer chains interact with the same nanotube. The relative polymer/nanotube density may influence in some way the stability of the helical state. For example, Smalley and coworkers[81] suggest multi-helical wrapping as the most likely configuration for PVP. Multi-helices have been experimentally observed in the P3HT case, as well[82]. In order to study the

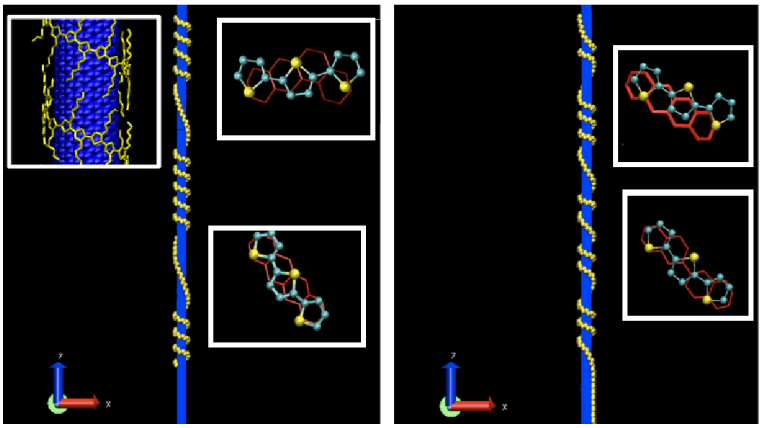

Figure 31: Polymer helical assembling on (15,0) zigzag (left) and (9,9) armchair (right) nanotubes after 0.5 ns at T= 300 K. Only the sulfur atoms are reported for clarity as yellow balls. The insets show the details of the interdigitation of the hexyl chains and the thiophene/nanotube lattice matching.

role of multiple chains a system containing one polymer chain (L = 64) helically wrapped on the nanotube (HH morphology) was used as a starting point, and a second chain was then added in two different ways: (i) wrapped along the nanotube next to the first one (see Fig. 32, left); (ii) unwrapped and parallel to the axis of the nanotube (see Fig. 32, right). The two geometries are considered in order to study the interaction of the wrapped chain with the structurally complex embedding polymer matrix in which the nanotubes are dispersed.

For both systems it is apparent that the second chain is able to stabilize the helical arrangement of the first chain, that is preserved at room temperature for the whole annealing time as long as 2 ns (final configurations of the systems are reported in Fig. 32). It is important to remark here that the same chain, whether isolated, unwraps in a time smaller than 0.5 ns. The relative polymer/nanotube density is accordingly a key factor which gives stability to the wrapped H morphology.

5.4 CONCLUSIONS

In conclusion, by molecular dynamics simulations on realistic long polymer chains, helical wrapping on single wall carbon nanotubes has been characterized. The helical wrapping

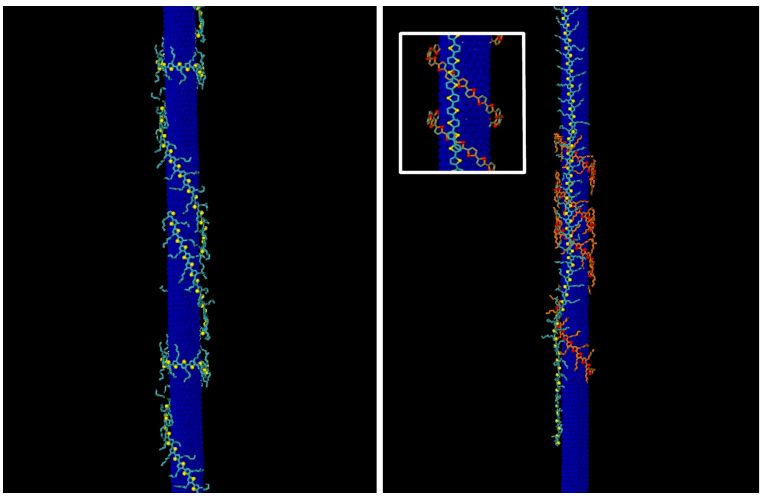

Figure 32: Two-chain polymer/nanotube systems after 2 ns annealing at room temperature. One chain is wrapped while the other is parallel to (right) or wrapped around (left) the nanotube. The inset shows the details of the superposition of the two chains (only thiophene rings shown for clarity).

in vacuo is found to be a metastable configuration stabilized by the interactions among neighboring polymer chains. It has been also shown that the nanotube chirality affects the actual coiling angles and morphology of the helix. We have enlightened that, since thermodynamic effects are important to understand polymer wrapping, we cannot limit our investigation to the calculation of the lowest energy structures, but long simulations at finite temperature must be performed. MPMD is a suitable computational tool which allows to take into account these effects. The introduction of other factors (such as e.g. the effect of different solvents on wrapping) can also be treated within this framework and will be the object of future work.

According to present study it is in principle possible to enhance the polymer-nanotube alignment so improving the polymer transport properties by a suitable tuning of temperature, polymer density and chain length. Polymer-nanotube systems are therefore still a promising technology for third-generation photovoltaics, provided that these factors are properly considered in the synthesis.

6

CONCLUSIONS

In this thesis we have studied via atomistic simulations hybrid and organic model systems formed by a polymer chain and a low dimension nanostructured acceptor with the aim to understand some important phenomena which are peculiar to nanostructured assemblies. Since accurate experimental characterization of the interfaces is difficult, atomistic simulations represent an important tool for a better understanding of the physical mechanisms at the nanoscale. We have extensively studied the P3HT wrapping on one-dimensional substrates such as carbon nanotubes and ZnO nanoneedles by means of model potential molecular dynamics, and we have identified the preferred polymer configurations. An important result obtained here is that even if in both systems an aligned configuration of the polymer chain is energetically favored, wrapped configurations can be found in real samples. Once the solvent has been dried, the wrapped configuration of P3HT on SWNT is metastable at room temperature, but the helical configurations induced by the synthesis procedure can be frozen by polymer-polymer interactions. Accordingly, it is in principle possible to enhance the polymer-nanotube alignment by a suitable tuning of the synthesis conditions, such as temperature, polymer density and chain length. Conversely, since the polymer mobility on the ZnO nanoneedles is low, in this case the energy barrier for the polymer diffusion on the surface is higher than on the SWNT, and the wrapping is stable at room temperature. The low dimensionality affects also the electronic and optical properties of the system: by studying a $Zn_{60}O_{60}$-6T model system, we have provided evidence of an electronic coupling between the organic and inorganic component which is originated by the nanocurvature of the semiconductor and which shifts the energy levels of the hybrid system. In particular, a comparison between the case of $Zn_{60}O_{60}$-6T with a previously reported study of sexithiophene on a flat $(10\bar{1}0)$ ZnO surface has been presented. While a type-II junction was found in the latter case, this staggered energy-level alignment is lost when the ZnO is nanostructured. Even if this effect may be reduced for larger ZnO nanoparticles, our results suggest a trend for the electronic level alignment at

the interface in nanostructured systems. ZnO nanoparticles of 120-atoms have been produced and proven to be particularly stable and abundant, thus they not only represent a model suitable for computational studies, but are also of potential technological interest. In order to understand their chemical structure, we have carried out a study which correlates their morphological and optoelectronic properties. We have calculated the absorption spectra of a set of $Zn_{60}O_{60}$ isomers in the near-middle ultraviolet: since the calculated spectra are different for each isomer, they represent an information which can be compared to experimental spectroscopic data to elucidate the most abundant structure of $Zn_{60}O_{60}$.

The results presented in this thesis suggest that, though the use of nanostructures in photovoltaic systems offers interesting advantages, such as the enhancement the donor/acceptor interface, it also requires deeper insight on the morphologies and electronic properties in order to improve the photovoltaic systems.

Part III

APPENDIX

A

COMPUTATIONAL FRAMEWORK

Contents

A.1 MODEL POTENTIAL MOLECULAR DYNAMICS CALCULATIONS

All molecular dynamics simulations were performed by using the DL_POLY parallel code[166]. The version used has changed in time (from 2.19 to 4.02) according to the most recent release. Common features of all the simulations performed are the use of periodic boundary conditions (applied in all directions), the choice of the integration algorithm and of the timestep: the equations of motion of atoms were integrated by using the Velocity Verlet algorithm with a timestep as small as 0.5 fs. Furthermore, in all the simulations carried out at constant temperature and volume, the temperature was controlled by the Berendsen thermostat with relaxation costant $f = 0.5$ ps, and all the electrostatic contributions were computed by the Ewald sum method with real space cutoff, $\rho_c = 8$ Å. In the constant pressure and temperature simulations, we used the Nosé-Hoover barostat with thermostat and barostat relaxation constants $f1_1 = 0.5$ and $f_2 = 0.1$ ps, respectively.

A.1.1 *Intramolecular forces*

The SWNTs, P_3HT and the nTs were described by the AMBER force field[167], that includes either bonding and non-bonding contributions. The bonding interactions are of three types. Eq.

14 describes the bond stretching potential, where r_{ij} is the atom-atom distance (see Fig.33).

$$U(r) = \frac{1}{2}k_b(r_{ij} - r_0)^2 \tag{14}$$

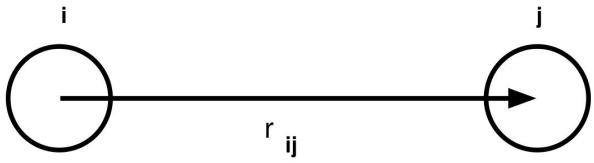

Figure 33: Interatomic bond vector.

Eq. 15 is the valence angle potential, where θ is the angle between the vectors connecting atom i to atom j and atom k. It describes the bond bending (see Fig.34).

$$U(\theta) = \frac{1}{2}k_a(\theta - \theta_0)^2 \tag{15}$$

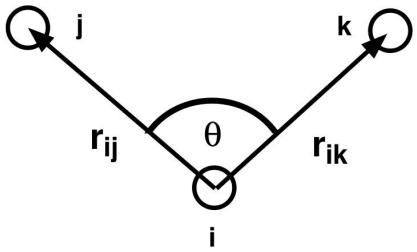

Figure 34: Valence angle.

The torsional (dihedral angle) potential is described in Eq. 16, where ϕ is the angle between the plane of atoms n,k,j and the vector connecting atom i to atom j (see Fig.35).

$$U(\phi) = A[1 + \cos(m\phi_{i-jkn} - \delta)] \tag{16}$$

The dispersive (i.e. Van der Waals) interactions are described by the sum of two-body Lennard-Jones contributions, as described in Eq. 17 (with Amber force field parameters)

$$U(r) = 4\epsilon\left[\left(\frac{\sigma}{r}\right)^{12} - \left(\frac{\sigma}{r}\right)^{6}\right] = \epsilon\left[\left(\frac{r_m}{r}\right)^{12} - 2\left(\frac{r_m}{r}\right)^{6}\right] \tag{17}$$

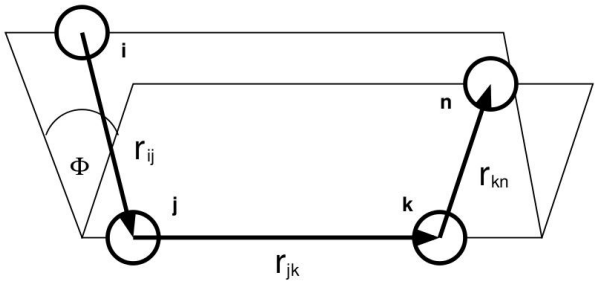

Figure 35: Dihedral angle.

where ϵ is the depth of the potential well, σ is the finite distance at which the inter-particle potential is zero, r is the distance between the particles, and r_m is the distance at which the potential reaches its minimum. The electrostatic contributions are described by a classical Coulomb term. The standard AM1-CM2 method[168] was applied to calculate the atomic partial charges.

The interatomic potential for Zn-O forces was described as the sum of an electrostatic term plus a Buckingham-type contribution[45]

$$E_{Zn-O}(r_{ij}) = \frac{q_i q_j}{r_{ij}} + A \cdot exp\left(\frac{-r_{ij}}{\rho}\right) - \frac{C}{r_{ij}^6} \qquad (18)$$

where r_{ij} is the distance between i and j ions, q_i and q_j are the charges on ions i and j, respectively, and A, ρ and C are the potential parameters, which were all taken from Ref.[45].

A.1.2 *Intermolecular forces*

The dispersive interactions between the polymer and the SWNT or the ZnO nanoneedle/nanocluster were described by a Lennard-Jones potential (Eq.17) as in Ref.[169], while the electrostatic contributions are represented by a simple Coulomb term.

A.2 DENSITY FUNCTIONAL THEORY CALCULATIONS

Ground-state DFT calculations were all performed with the quantum chemistry program package TURBOMOLE[170]. The electronic wavefunctions were represented using a Gaussian orbital basis set of split valence triple–ζ quality augmented with polarization functions (TZVP)[171]. In all cases, the resolution of

identity approximation was adopted for computing the electronic Coulomb interaction[172]: this usually leads to a more than tenfold speedup of the calculations, without sacrificing accuracy. In addition, the multipole accelerated resolution of identity approximation[173] was used, enabling even more efficient calculations. In each SCF cycle, the energy was required to be converged within $3 \cdot 10^{-6}$ eV and the grid for numerical evaluation of the exchange-correlation operator was set to medium size[174]. The dispersive van der Waals interactions were included by applying the Grimme correction[115,117], and adhesion energies were corrected for the basis-set superposition error using the counterpoise method[175].

For the ZnO-nTs system, the PBE exchange-correlation (XC) functional[151] was used to model the exchange-correlation energy, while for the $(ZnO)_{60}$ isomers the gradient-corrected BP86 XC functional[176–178] was chosen.

A.2.1 *Time dependent DFT calculations*

The TDDFT calculations on the $(ZnO)_{60}$ isomers were performed using the single-valence SVP basis set in conjunction with the modified B3LYP[179] functional (with 27.5% Hartree-Fock exchange), which has proven to give good results for ZnO clusters[144]. TDDFT calculations were performed in water solution, by means of the Conductor-like Polarizable Continuum Model of solvation (C-PCM)[180], used in its non-equilibrium version[181]. All hybrid DFT calculations have been performed using the Gaussian 09 program package[182].

LIST OF FIGURES

LIST OF TABLES

BIBLIOGRAPHY

[1] P. V. Kamat, "Meeting the clean energy demand: Nanostructure architectures for solar energy conversion," *The Journal of Physical Chemistry C*, vol. 111, no. 7, pp. 2834–2860, 2007. (Cited on page 3.)

[2] National Renewable Energy Labs. http://www.nrel.gov/ncpv/. (Cited on pages 3, 4, and 75.)

[3] M. A. Green, K. Emery, Y. Hishikawa, W. Warta, and E. D. Dunlop, "Solar cell efficiency tables (version 39)," *Progress in Photovoltaics: Research and Applications*, vol. 20, no. 1, pp. 12–20, 2012. (Cited on page 3.)

[4] N. Espinosa, M. Hosel, D. Angmo, and F. C. Krebs, "Solar cells with one-day energy payback for the factories of the future," *Energy Environ. Sci.*, vol. 5, pp. 5117–5132, 2012. (Cited on page 3.)

[5] P. Jackson, D. Hariskos, E. Lotter, S. Paetel, R. Wuerz, R. Menner, W. Wischmann, and M. Powalla, "New world record efficiency for Cu(In,Ga)Se2 thin-film solar cells beyond 20%," *Progress in Photovoltaics: Research and Applications*, vol. 19, no. 7, pp. 894–897, 2011. (Cited on page 3.)

[6] B. R. Saunders and M. L. Turner, "Nanoparticle-polymer photovoltaic cells," *Advances in Colloid and Interface Science*, vol. 138, no. 1, pp. 1 – 23, 2008. (Cited on page 3.)

[7] M. Wright and A. Uddin, "Organic-inorganic hybrid solar cells: a comparative review," *Solar energy materials & solar cells*, vol. 107, pp. 87–111, 2012. (Cited on pages 3 and 5.)

[8] S. Monticone, R. Tufeu, and Kanaev, "Complex nature of the UV and visible fluorescence of colloidal ZnO nanoparticles," *J. Phys. Chem. B*, vol. 102, no. 16, pp. 2854–2862, 1998. (Cited on pages 4 and 52.)

[9] C. Piliego, M. Manca, R. Kroon, M. Yarema, K. Szendrei, M. R. Andersson, W. Heiss, and M. A. Loi, "Charge separation dynamics in a narrow band gap polymer-pbs nanocrystal blend for efficient hybrid solar cells," *J. Mater.*

Chem., vol. 22, pp. 24411–24416, 2012. (Cited on pages 4 and 7.)

[10] F. C. Krebs, "Processing and preparation of polymer and organic solar cells," *Solar Energy Materials and Solar Cells*, vol. 93, no. 4, pp. 393 –, 2009. (Cited on pages 4 and 5.)

[11] T. T. Larsen-Olsen, B. Andreasen, T. R. Andersen, A. P. Böttiger, E. Bundgaard, K. Norrman, J. W. Andreasen, M. J. rgensen, and F. C. Krebs, "Simultaneous multilayer formation of the polymer solar cell stack using roll-to-roll double slot-die coating from water," *Solar Energy Materials and Solar Cells*, vol. 97, no. 0, pp. 22 – 27, 2012. (Cited on page 4.)

[12] H.-Y. Chen, J. Hou, S. Zhang, Y. Liang, G. Yang, Y. Yang, L. Yu, Y. Wu, , and G. Li, "Polymer solar cells with enhanced open-circuit voltage and efficiency," *Nat. Photon.*, pp. 649 – 653, 2009. (Cited on page 4.)

[13] J. Peet, J. Y. Kim, N. E. Coates, W. L. Ma, D. Moses, A. J. Heeger, and G. C. Bazan, "Efficiency enhancement in low-bandgap polymer solar cells by processing with alkane dithiols," *Nat. Mater.*, vol. 6, pp. 497–500, 2007. (Cited on page 4.)

[14] M. T. Dang, L. Hirsch, and G. Wantz, "P3HT:PCBM, best seller in polymer photovoltaic research," *Advanced Materials*, vol. 23, no. 31, pp. 3597–3602, 2011. (Cited on page 4.)

[15] B. Pradhan, K. Setyowati, H. Liu, D. H. Waldeck, and J. Chen, "Carbon nanotube - polymer nanocomposite infrared sensor," *Nano Lett.*, vol. 8, pp. 1142–1146, 2008. (Cited on page 4.)

[16] G. K. Mor, S. Kim, M. Paulose, O. K. Varghese, K. Shankar, J. e. Basham, and C. A. Grimes, "Visible to near-infrared light harvesting in TiO2 nanotube array-P3HT based heterojunction solar cells," *Nano Letters*, vol. 9, no. 12, pp. 4250–4257, 2009. PMID: 19775127. (Cited on page 4.)

[17] M. T. Lloyd, R. P. Prasankumar, M. B. Sinclair, A. C. Mayer, D. C. Olson, and J. W. P. Hs u, "Impact of interfacial polymer morphology on photoexcitation dynamics and device performance in P3HT/ZnO heterojunctions," *J. Mater. Chem.*, vol. 19, pp. 4609–4614, 2009. (Cited on pages 4 and 11.)

[18] G. Dennler, M. C. Scharber, and C. J. Brabec, "Polymer-fullerene bulk-heterojunction solar cells," *Advanced Materials*, vol. 21, no. 13, pp. 1323–1338, 2009. (Cited on page 5.)

[19] Y.-W. Su, S.-C. Lan, and K.-H. Wei, "Organic photovoltaics," *Materials Today*, vol. 15, no. 12, pp. 554 – 562, 2012.

[20] Y.-S. Zimmermann, A. Schäffer, C. Hugi, K. Fent, P. F.-X. Corvini, and M. Lenz, "Organic photovoltaics: Potential fate and effects in the environment," *Environment International*, vol. 49, no. 0, pp. 128 – 140, 2012.

[21] A. Marrocchi, D. Lanari, A. Facchetti, and L. Vaccaro, "Poly(3-hexylthiophene): synthetic methodologies and properties in bulk heterojunction solar cells," *Energy Environ. Sci.*, vol. 5, pp. 8457–8474, 2012. (Cited on page 5.)

[22] D. C. Olson, J. Piris, R. T. Collins, S. E. Shaheen, and D. S. Ginley, "Hybrid photovoltaic devices of polymer and ZnO nanofiber composites," *Thin Solid Films*, vol. 496, no. 1, pp. 26 – 29, 2006. Proceedings of the Fourth International Symposium on Transparent Oxide Thin Films for Electronics and Optics (TOEO-4). (Cited on pages 5, 7, and 19.)

[23] J. A. Cheng, J. H. Rhee, S. H. Im, Y. H. Lee, H. jung Kim, S. I. Seok, M. K. Nazeeruddin, and M. Grätzel, "High-performance nanostructured inorganic-organic heterojunction solar cells," *Nano Lett.*, vol. 10, pp. 2609–2612, 2010. (Cited on page 5.)

[24] P. B. e. H. Sirringhaus, "Two-dimensional charge transport in self-organized, high-mobility conjugated polymers," *Nature*, vol. 401, pp. 685–688, 1999. (Cited on page 5.)

[25] G. Horowitz, "Organic field-effect transistors," *Advanced Materials*, vol. 10, no. 5, pp. 365–377, 1998. (Cited on page 5.)

[26] C. Vijila, A. Pivrikas, H. Chun, C. Zhikuan, and R. "A study of charge transport in a novel electroluminescent poly(phenylene vinylene-co-fluorenylene vinylene) based conjugated π-polymer," *Organic Electronics*, vol. 8, no. 1, pp. 8 – 13, 2007. (Cited on page 5.)

[27] C.-K. Lee and C.-W. P. abd Chun-Wei Chen, "Correlation of nanoscale organizations of polymer and nanocrystals in polymer/inorganic nanocrystal bulk heterojunction hybrid solar cells: insights from multiscale molecular simulations," *Energy Environ. Sci.*, vol. 6, pp. 307–315, 2013. (Cited on page 5.)

[28] A. J. Ferguson, J. L. Blackburn, and N. Kopidakis, "Fullerenes and carbon nanotubes as acceptor materials in organic photovoltaics," *Materials Letters*, vol. 90, no. 0, pp. 115 – 125, 2013. (Cited on page 5.)

[29] A. Javey, J.Guo, Q. Wang, M. Lundstrom, and H. Dai, "Ballistic carbon nanotube field-effect transistors," *Nature*, vol. 424, pp. 654–657, 2003. (Cited on page 5.)

[30] R. C. Tenent, T. M. Barnes, J. D. Bergeson, A. J. Ferguson, B. To, and L. M. G. et. al, "Ultrasmooth, large-area, high-uniformity, conductive transparent single-walled-carbon-nanotube films for photovoltaics produced by ultrasonic spraying," *Adv. Mater.*, pp. 3210–3216, 2009. (Cited on page 5.)

[31] T. Dürkop, S. A. Getty, E. Cobas, and M. S. Fuhrer, "Extraordinary mobility in semiconducting carbon nanotubes," *Nano Lett.*, vol. 4, pp. 35–39, 2004. (Cited on page 5.)

[32] S. Kazaoui, N. Minami, B. Nalini, Y. Kim, and K. Hara, "Near-infrared photoconductive and photovoltaic devices using single-wall carbon nanotubes in conductive polymer films," *Journal of Applied Physics*, vol. 98, no. 8, p. 084314, 2005. (Cited on page 5.)

[33] M. Lanzi, L. Paganin, and D. Caretti, "New photoactive oligo- and poly-alkylthiophenes," *Polymer*, vol. 49, no. 23, pp. 4942 – 4948, 2008. (Cited on page 5.)

[34] G. Zhang, P. Qi, X. Wang, Y. Lu, X. Li, R. Tu, S. Bangsaruntip, D. Mann, L. Zhang, and H. Dai, "Selective etching of metallic carbon nanotubes by gas-phase reaction," *Science*, vol. 314, no. 5801, pp. 974–977, 2006. (Cited on page 5.)

[35] R. E. Smalley, Y. Li, V. C. Moore, B. K. Price, R. Colorado, H. K. Schmidt, R. H. Hauge, A. R. Barron, and J. M. Tour, "Single wall carbon nanotube amplification: En route to a

type-specific growth mechanism," *Journal of the American Chemical Society*, vol. 128, no. 49, pp. 15824–15829, 2006. PMID: 17147393.

[36] L. Ding, A. Tselev, J. Wang, D. Yuan, H. Chu, T. P. McNicholas, Y. Li, and J. Liu, "Selective growth of well-aligned semiconducting single-walled carbon nanotubes," *Nano Letters*, vol. 9, no. 2, pp. 800–805, 2009. PMID: 19159186.

[37] G. Hong, B. Zhang, B. Peng, J. Zhang, W. M. Choi, J.-Y. Choi, J. M. Kim, and Z. Liu, "Direct growth of semiconducting single-walled carbon nanotube array," *Journal of the American Chemical Society*, vol. 131, no. 41, pp. 14642–14643, 2009. PMID: 19778018. (Cited on page 5.)

[38] P. G. Collins, M. S. Arnold, and P. Avouris, "Engineering carbon nanotubes and nanotube circuits using electrical breakdown," *Science*, vol. 292, no. 5517, pp. 706–709, 2001. (Cited on page 5.)

[39] D. Chattopadhyay, I. Galeska, and F. Papadimitrakopoulos, "A route for bulk separation of semiconducting from metallic single-wall carbon nanotubes," *Journal of the American Chemical Society*, vol. 125, no. 11, pp. 3370–3375, 2003.

[40] T. Tanaka, H. Jin, Y. Miyata, S. Fujii, H. Suga, Y. Naitoh, T. Minari, T. Miyadera, K. Tsukagoshi, and H. Kataura, "Simple and scalable gel-based separation of metallic and semiconducting carbon nanotubes," *Nano Letters*, vol. 9, no. 4, pp. 1497–1500, 2009.

[41] H. W. e. Lee, "Selective dispersion of high purity semiconducting single-walled carbon nanotubes with regioregular poly(3-alkylthiophene)s," *Nat. Commun.*, p. 541, 2011. (Cited on page 5.)

[42] X. Fang, M. Cao, and X. S. et al., "Microwave responses and general model of nanotetraneedle ZnO: Integration of interface scattering, microcurrent, dielectric relaxation, and microantenna," *J. Appl. Pys.*, vol. 107, p. 054304, 2010. (Cited on pages 6 and 7.)

[43] M. H. Huang, Y. Y. Wu, H. Feick, N. Tran, E. Weber, and P. D. Yang, "Catalytic growth of zinc oxide nanowires by vapor transport," *Adv. Mater*, vol. 13, pp. 113–116, 2001.

[44] M. J. Zheng, L. D. Zhang, G. H. Li, and W. Z. Shen, "Fabrication and optical properties of large-scale uniform zinc oxide nanowire arrays by one-step electrochemical deposition technique," *Chem. Phys. lett.*, vol. 363, pp. 123–128, 2002. (Cited on pages 6 and 7.)

[45] A. J. Kullkarni, M. Zhou, and F. J. Ke, "Orientation and size dependence of the elastic properties of zinc oxide nanobelts," *Nanotechnology*, vol. 16, pp. 2749–2756, 2005. (Cited on pages 6, 11, 19, 44, and 73.)

[46] L. W. Ji, W. S. Shih, T. H. Fang, C. Z. Wu, S. M. Peng, and T. H. Meen, "Preparation and characteristics of hybrid ZnO-polymer solar cells," *J. Mat. Sci.*, vol. 45, pp. 3266–3269, 2010. (Cited on pages 6, 7, 11, and 19.)

[47] D. Look, D. Reynolds, J. Sizelove, R. Jones, C. Litton, G. Cantwell, and W. Harsch, "Electrical properties of bulk ZnO," *Solid State Communications*, vol. 105, no. 6, pp. 399 – 401, 1998. (Cited on page 6.)

[48] J. Weickert, R. B. Dunbar, H. C. Hesse, W. Wiedemann, and L. Schmidt-Mende, "Nanostructured organic and hybrid solar cells," *Advanced Materials*, vol. 23, no. 16, pp. 1810–1828, 2011. (Cited on page 6.)

[49] F. C. Krebs and K. Norrman, "Analysis of the failure mechanism for a stable organic photovoltaic during 10000 h of testing," *Progress in Photovoltaics: Research and Applications*, vol. 15, no. 8, pp. 697–712, 2007. (Cited on page 6.)

[50] K. Norrman, S. A. Gevorgyan, and F. C. Krebs, "Water-induced degradation of polymer solar cells studied by H218O labeling," *ACS Applied Materials & Interfaces*, vol. 1, no. 1, pp. 102–112, 2009. PMID: 20355761. (Cited on page 6.)

[51] A. Göpferich, "Mechanisms of polymer degradation and erosion," *Biomaterials*, vol. 17, no. 2, pp. 103 – 114, 1996. (Cited on page 6.)

[52] M. J. rgensen, K. Norrman, and F. C. Krebs, "Stability/degradation of polymer solar cells," *Solar Energy Materials and Solar Cells*, vol. 92, no. 7, pp. 686 – 714, 2008. (Cited on page 6.)

[53] U. Özgür, Y. Alivov, C. Liu, and et al., "A comprehensive review of ZnO materials and devices," *J. Appl. Phys.*, vol. 98, pp. 1–103, 2005. (Cited on page 6.)

[54] D. C. Cronemeyer, "Electrical and optical properties of rutile single crystals," *Phys. Rev.*, vol. 87, pp. 876–886, 1952. (Cited on page 6.)

[55] M. Grätzel, "Photoelectrochemical cells," *Nature*, vol. 414, pp. 338–344, 2001. (Cited on page 6.)

[56] J. Preat, D. Jacquemin, and E. A. Perpete, "Towards new efficient dye-sensitised solar cells," *Energy Environ. Sci.*, vol. 3, pp. 891–904, 2010.

[57] J. N. Clifford, E. Martinez-Ferrero, A. Viterisi, and E. Palomares, "Sensitizer molecular structure-device efficiency relationship in dye sensitized solar cells," *Chem. Soc. Rev.*, vol. 40, pp. 1635–1646, 2011. (Cited on page 6.)

[58] M. Grätzel, "Dye-sensitized solid-state heterojunction solar cells," *MRS Bulletin*, vol. 30. (Cited on page 6.)

[59] T. Taguchi, X.-t. Zhang, I. Sutanto, K.-i. Tokuhiro, T. N. Rao, H. Watanabe, T. Nakamori, M. Uragami, and A. Fujishima, "Improving the performance of solid-state dye-sensitized solar cell using MgO-coated TiO2 nanoporous film," *Chem. Commun.*, vol. 0, pp. 2480–2481, 2003. (Cited on page 6.)

[60] J. Bandara and H. Weerasinghe, "Solid-state dye-sensitized solar cell with p-type nio as a hole collector," *Solar Energy Materials and Solar Cells*, vol. 85, no. 3, pp. 385 – 390, 2005. (Cited on page 6.)

[61] I. Chung, B. Lee, J. He, R. P. H. Chang, and M. G. Kanatzidis, "All-solid-state dye-sensitized solar cells with high efficiency," *Nature*, vol. 485, pp. 486–489, 2012. (Cited on page 6.)

[62] A. Yella, H.-W. Lee, H. N. Tsao, C. Yi, A. K. Chandiran, M. Nazeeruddin, E. W.-G. Diau, C.-Y. Yeh, S. M. Zakeeruddin, and M. Grätzel, "Porphyrin-sensitized solar cells with cobalt (II/III)-based redox electrolyte exceed 12 percent efficiency," *Science*, vol. 334, no. 6056, pp. 629–634, 2011. (Cited on page 6.)

[63] H. Fu and S.-W. Tsang, "Infrared colloidal lead chalcogenide nanocrystals: Synthesis, properties, and photovoltaic applications," *Nanoscale*, vol. 4, pp. 2187–2201, 2012. (Cited on page 7.)

[64] K. M. Noone, E. Strein, N. C. Anderson, P.-T. Wu, S. A. Jenekhe, and D. S. Ginger, "Broadband absorbing bulk heterojunction photovoltaics using low-bandgap solution-processed quantum dots," *Nano Letters*, vol. 10, no. 7, pp. 2635–2639, 2010. (Cited on page 7.)

[65] A. Said, G. Poize, C. Martini, and et al., "Hybrid bulk heterojunction solar cells based on P3HT and porphyrin-modified ZnO nanorods," *J. Phys. Chem. C*, vol. 114, pp. 11273–11278, 2010. (Cited on pages 7 and 75.)

[66] A. L. Briseno, T. W. Holcombe, A. I. Boukai, E. C. Garnett, S. W. Shelton, J. J. M. Fréchet, and P. Yang, "Oligo-and polythiophene/ZnO hybrid nanowire solar cells," *Nano Lett.*, vol. 10, pp. 334–340, 2010. (Cited on page 7.)

[67] W. Beek, M. Wienk, and R. Janssen, "Hybrid solar cells from regioregular polythiophene and ZnO nanoparticles," *Advanced Functional Materials*, vol. 16, no. 8, pp. 1112–1116, 2006. (Cited on page 7.)

[68] P. A. C. Quist, W. J. E. Beek, M. M. Wienk, R. A. J. Janssen, T. J. Savenije, and L. D. A. Siebbeles, "Photogeneration and decay of charge carriers in hybrid bulk heterojunctions of ZnO nanoparticles and conjugated polymers," *The Journal of Physical Chemistry B*, vol. 110, no. 21, pp. 10315–10321, 2006. PMID: 16722734.

[69] N. C. Das and P. E. Sokol, "Hybrid photovoltaic devices from regioregular polythiophene and ZnO nanoparticles composites," *Renewable Energy*, vol. 35, no. 12, pp. 2683 – 2688, 2010. (Cited on page 7.)

[70] J. Xie, P. Li, Y. Wang, and et al., "Synthesis of ZnO whiskers with different aspect ratios by a facile solution route," *Phys. Stat. Sol. A*, vol. 205, pp. 1560–1565, 2008. (Cited on page 7.)

[71] D. Lincot, "Solution growth of functional zinc oxide films and nanostructures," *MRS Bull.*, vol. 35, pp. 778–788, 2010. (Cited on page 7.)

[72] S. D. Oosterhout, M. M. Wienk, S. S. van Bavel, R. Thiedmann, L. J. A. Koster, J. Gilot, J. Loos, V. Schmidt, and R. A. Janssen, "The effect of three-dimensional morphology on the efficiency of hybrid polymer solar cells," *Nat. Mater.*, vol. 8, pp. 818–824, 2009. (Cited on pages 7, 9, and 12.)

[73] B. A. Gregg, "The photoconversion mechanism of excitonic solar cells," *MRS bull.*, vol. 30, pp. 20–22, 2005. (Cited on page 8.)

[74] P. E. Shaw, A. Ruseckas, and I. D. W. Samuel, "Exciton diffusion measurements in poly(3-hexylthiophene)," *Advanced Materials*, vol. 20, no. 18, pp. 3516–3520, 2008. (Cited on page 9.)

[75] M. Wang and X. Wang, "PPV/TiO2 hybrid composites prepared from ppv precursor reaction in aqueous media and their application in solar cells," *Polymer*, vol. 49, no. 6, pp. 1587 – 1593, 2008. (Cited on page 9.)

[76] W.-H. Baek, I. Seo, T.-S. Yoon, H. H. Lee, C. M. Yun, and Y.-S. Kim, "Hybrid inverted bulk heterojunction solar cells with nanoimprinted TiO2 nanopores," *Solar Energy Materials and Solar Cells*, vol. 93, no. 9, pp. 1587 – 1591, 2009. (Cited on page 9.)

[77] R. J. Kline, M. D. McGehee, and M. F. Toney, "Highly oriented crystals at the buried interface in polythiophene thin-film transistors," *Nat. Mater.*, vol. 5, pp. 222–228, 2006. (Cited on page 10.)

[78] F. C. Spano, "Modeling disorder in polymer aggregates: The optical spectroscopy of regioregular poly(3-hexylthiophene) thin films," *J. Chem. Phys.*, vol. 122, pp. 234701–15, 2005.

[79] J. Veres, S. Ogier, and G. Lloyd, "Gate insulators in organic field-effect transistors," *Chem. Mater.*, vol. 16, pp. 4543 – 4555, 2004. (Cited on page 10.)

[80] C. Park, Z. Ounaies, K. A. Watson, R. E. Crooks, J. Smith, S. E. Lowther, J. W. Connell, E. J. Siochi, J. S. Harrison, and T. L. S. Clair, "Dispersion of single wall carbon nanotubes by in situ polymerization under sonication," *Chem. Phys. Lett.*, vol. 364, pp. 303–308, 2002. (Cited on pages 10 and 57.)

[81] M. J. O'Connel, P. Boul, L. M. Ericson, C. H. an Yuhuang Wang, E. Haroz, C. Kuper, J. Tour, K. D. Ausman, and R. E. Smalley, "Reversible water-solubilization of single-walled carbon nanotubes by polymer wrapping," *Chem. Phys. Lett.*, vol. 342, pp. 265–271, 2001. (Cited on pages 10, 57, and 64.)

[82] M. Giulianini, E. R. Waclawik, J. M. Bell, M. De Crescenzi, P. Castrucci, M. Scarselli, and N. Motta, "Regioregular poly(3-hexyl-thiophene) helical self-organization on carbon nanotubes," *Appl. Phys. Lett.*, vol. 95, 2009. (Cited on pages 10, 11, 57, 58, 60, 63, 64, and 75.)

[83] J. Gao, M. Loi, E. Figueiredo de Carvalho, and M. dos Santos, "Selective wrapping and supramolecular structures of polyfluorene-carbon nanotube hybrids," *ACS Nano*, vol. 5, no. 5, pp. 3993–3999, 2011. (Cited on pages 11, 31, and 75.)

[84] J. W. Hsu and M. T. Lloyd, "Organic/inorganic hybrids for solar energy generation," *MRS Bull.*, vol. 422, p. 234701, 2010. (Cited on page 11.)

[85] X. C. Chen and P. F. Green, "Control of morphology and its effects on the optical properties of polymer nanocomposites," *Langmuir*, vol. 26, no. 5, pp. 3659–3665, 2010. PMID: 19957937. (Cited on page 11.)

[86] Y. Wei, B. R. Hseih, M. E. Galvin, and A. C. Society, *Semiconducting polymers : applications, properties, and synthesis*. Washington, DC : American Chemical Society, 1999.

[87] Z. Xu, H. Tsai, H.-L. Wang, and M. Cotlet, "Solvent polarity effect on chain conformation, film morphology, and optical properties of a water-soluble conjugated polymer," *The Journal of Physical Chemistry B*, vol. 114, no. 36, pp. 11746–11752, 2010. (Cited on page 11.)

[88] D. P. McMahon, D. L. Cheung, and A. Troisi, "Why holes and electrons separate so well in polymer/fullerene photovoltaic cells," *The Journal of Physical Chemistry Letters*, vol. 2, no. 21, pp. 2737–2741, 2011. (Cited on page 11.)

[89] M. Scharber, D. Mühlbacher, M. Koppe, P. Denk, C. Waldauf, A. Heeger, and C. Brabec, "Design rules for donors

in bulk-heterojunction solar cells-towards 10% energy-conversion efficiency," *Advanced Materials*, vol. 18, no. 6, pp. 789–794, 2006. (Cited on page 11.)

[90] I. Avilov, V. Geskin, and J. Cornil, "Quantum-chemical characterization of the origin of dipole formation at molecular organic/organic interfaces," *Advanced Functional Materials*, vol. 19, no. 4, pp. 624–633, 2009. (Cited on page 12.)

[91] H. Ishii, K. Sugiyama, E. Ito, and K. Seki, "Energy level alignment and interfacial electronic structures at organic/metal and organic/organic interfaces," *Advanced Materials*, vol. 11, no. 8, pp. 605–625, 1999. (Cited on page 12.)

[92] J.-L. Brédas, J. E. Norton, J. Cornil, and V. Coropceanu, "Molecular understanding of organic solar cells: The challenges," *Accounts of Chemical Research*, vol. 42, no. 11, pp. 1691–1699, 2009. (Cited on page 12.)

[93] L. Zhang and H. Huang, "Structural transformation of ZnO nanostructures," *Appl. Phys. Lett.*, vol. 90, p. 2431073, 2007.

[94] H. Wei, J. Li, Y. Cai, Z. Xu, S. Lee, Y. Li, and J. Tang, "Electronic structures of planar and mixed c70/cupc heterojunctions in organic photovoltaic devices," *Organic Electronics*, vol. 12, no. 8, pp. 1422 – 1428, 2011. (Cited on pages 12 and 75.)

[95] E. V. Canesi, M. Binda, A. Abate, S. Guarnera, L. Moretti, V. D'Innocenzo, R. Sai Santosh Kumar, C. Bertarelli, A. Abrusci, H. Snaith, A. Calloni, A. Brambilla, F. Ciccacci, S. Aghion, F. Moia, R. Ferragut, C. Melis, G. Malloci, A. Mattoni, G. Lanzani, and A. Petrozza, "The effect of selective interactions at the interface of polymer-oxide hybrid solar cells," *Energy Environ. Sci.*, vol. 5, pp. 9068–9076, 2012. (Cited on page 12.)

[96] D. Kuroda, H. Shirai, M. P. Jacobson, and H. Nakamura, "Computer-aided antibody design," *Protein Engineering Design and Selection*, vol. 25, no. 10, pp. 507–522, 2012. (Cited on page 13.)

[97] F. Collu, A. V. Vargiu, J. Dreier, M. Cascella, and P. Ruggerone, "Recognition of imipenem and meropenem by

the rnd-transporter mexb studied by computer simulations," *Journal of the American Chemical Society*, vol. 134, no. 46, pp. 19146–19158, 2012. (Cited on page 13.)

[98] A. Mattoni, M. Ippolito, and L. Colombo, "Atomistic modeling of brittleness in covalent materials," *Phys. Rev. B*, vol. 76, p. 224103, 2007. (Cited on page 13.)

[99] N. Pugno, A. Carpinteri, M. Ippolito, A. Mattoni, and L. Colombo, "Atomistic fracture: QFM vs. MD," *Engineering Fracture Mechanics*, vol. 75, no. 7, pp. 1794 – 1803, 2008. Critical Distance Theories of Fracture. (Cited on page 13.)

[100] Y. Sakiyama, S. Takagi, and Y. Matsumoto, "Validation of intermolecular pair potential model of SiH_4: Molecular-dynamics simulation for saturated liquid density and thermal transport properties," *The Journal of Chemical Physics*, vol. 122, no. 23, p. 234501, 2005. (Cited on page 13.)

[101] P. V. Komarov, Y.-T. Chiu, S.-M. Chen, and P. Reineker, "Investigation of thermal expansion of polyimide/SiO_2 nanocomposites by molecular dynamics simulations," *Macromolecular Theory and Simulations*, vol. 19, no. 1, pp. 64–73, 2010. (Cited on page 13.)

[102] B. Li, D. Xu, X. Zhang, Z. Jiang, Y. Wang, J. Ma, X. Dong, and H. Wu, "Rubbery polymer-inorganic nanocomposite membranes: Free volume characteristics on separation property," *Industrial & Engineering Chemistry Research*, vol. 49, no. 24, pp. 12444–12451, 2010. (Cited on page 13.)

[103] C. Melis, A. Mattoni, and L. Colombo, "Atomistic investigation of poly(3-hexylthiophene) adhesion on nanostructured titania," *J. Phys. Chem. C*, vol. 114, pp. 3401–3406, 2010. (Cited on pages 13 and 24.)

[104] M. Alves-Santos and M. J. Caldas, "Classical simulation of deposition of thiophene oligomers on TiO2-anatase: Relevance of long-range electrostatic interactions," *Synthetic Metals*, vol. 159, no. 21-22, pp. 2302–2305, 2009. (Cited on page 13.)

[105] M. I. Saba, C. Melis, L. Colombo, G. Malloci, and A. Mattoni, "Polymer crystallinity and transport properties at the poly(3-hexylthiophene)/zinc oxide interface," *J. Phys.*

Chem. C, vol. 115, no. 19, pp. 9651–9655, 2011. (Cited on page 13.)

[106] J. P. Perdew and M. Levy, "Physical content of the exact kohn-sham orbital energies: Band gaps and derivative discontinuities," *Phys. Rev. Lett.*, vol. 51, pp. 1884–1887, 1983. (Cited on page 14.)

[107] F. Bechstedt, R. del Sole, G. Cappellini, and L. Reining, "An efficient method for calculating quasiparticle energies in semiconductors," *Sol. St. Commun.*, vol. 84, 1992. (Cited on page 14.)

[108] N. Sai, K. Leung, and J. Chelikowsky, "Hybrid density functional study of oligothiophene/ZnO interface for photovoltaics," *Phys. Rev. B*, vol. 83, p. 121309(R), 2011. (Cited on pages 14, 32, 36, and 38.)

[109] R. O. Jones and O. Gunnarsson, "The density functional formalism, its applications and prospects," *Rev. Mod. Phys.*, vol. 61, pp. 689–746, 1989. (Cited on pages 14 and 33.)

[110] J. Gavnholt, T. Olsen, M. Engelund, and J. S. tz, "Δ self-consistent field method to obtain potential energy surfaces of excited molecules on surfaces," *Phys. Rev. B*, vol. 78, p. 075441, 2008. (Cited on page 14.)

[111] T. Kowalczyk, S. R. Yost, , and T. V. Voorhis, "Assessment of the ΔSCF density functional theory approach for electronic excitations in organic dyes," *J. Chem. Phys.*, vol. 134, p. 054128, 2011.

[112] G. Malloci, G. Mulas, G. Cappellini, and C. Joblin, "Time-dependent density functional study of the electronic spectra of oligoacenes in the charge states -1, 0, +1 and +2," *Chem. Phys.*, vol. 340, pp. 43–58, 2007. (Cited on page 14.)

[113] A. Calzolari, A. Ruini, and A. Catellani, "Anchor group versus conjugation: Toward the gap-state engineering of functionalized ZnO(10$\bar{1}$0) surface for optoelectronic applications," *Journal of the American Chemical Society*, vol. 133, no. 15, pp. 5893–5899, 2011. (Cited on page 14.)

[114] F. De Angelis, S. Fantacci, and A. Sgamellotti, "An integrated computational tool for the study of the optical properties of nanoscale devices: application to solar

cells and molecular wires," *Theoretical Chemistry Accounts*, vol. 117, pp. 1093–1104, 2007. (Cited on page 14.)

[115] A. Tkatchenko, L. Romaner, O. T. Hofmann, E. Zojer, C. Ambrosch-Draxl, and M. Scheffler, "Van der Waals interactions between organic adsorbates and at organic/inorganic interfaces," *MRS Bull.*, vol. 35, pp. 435–442, 2010. (Cited on pages 14 and 74.)

[116] M. Dion, H. Rydberg, E. Schröder, D. C. Langreth, and B. I. Lundqvist, "Van der waals density functional for general geometries," *Phys. Rev. Lett.*, vol. 92, p. 246401, 2004. (Cited on page 14.)

[117] S. Grimme, "Semiempirical ggc-type density functional constructed with a long-range dispersion contribution," *J. Comput. Chem.*, vol. 27, pp. 1787–1799, 2006. (Cited on pages 14 and 74.)

[118] P. Jurečka, J. Černý, P. Hobza, and D. R. Salahub, "Density functional theory augmented with an empirical dispersion term. interaction energies and geometries of 80 noncovalent complexes compared with ab initio quantum mechanics calculations," *Journal of Computational Chemistry*, vol. 28, no. 2, pp. 555–569, 2007.

[119] A. Tkatchenko and M. Scheffler, "Accurate molecular van der waals interactions from ground-state electron density and free-atom reference data," *Phys. Rev. Lett.*, vol. 102, p. 073005, 2009. (Cited on page 14.)

[120] P. Ravirajan, A. M. Peiró, M. K. Nazeeruddin, M. Graetzel, D. D. C. Bradley, J. R. Durrant, and J. Nelson, "Hybrid polymer/zinc oxide photovoltaic devices with vertically oriented ZnO nanorods and an amphiphilic molecular interface layer," *J. Phys. Chem. B*, vol. 110, no. 15, pp. 7635–7639, 2006. PMID: 16610853. (Cited on page 19.)

[121] C. Caddeo, R. Dessì, C. Melis, L. Colombo, and A. Mattoni, "Poly(3-hexylthiophene) adhesion on zinc oxide nanoneedles," *J. Phys. Chem. C*, vol. 115, pp. 16833 – 16837, 2011. (Cited on page 20.)

[122] M. Yin, Y. Gu, I. L. Kuskovsky, T. Andelman, Y. Zhu, G. F. Neumark, and S. O'Brien, "Zinc oxide quantum rods," *Journal of the American Chemical Society*, vol. 126, no. 20, pp. 6206–6207, 2004. (Cited on page 20.)

[123] S. Mutlu and B. G. Sonmez, "A solution state diode using semiconductor polymer nanorods with nanogap electrodes," *Nanotechnology*, vol. 23, no. 24, p. 245203, 2012. (Cited on page 21.)

[124] M. Al-Ibrahim, H.-K. Roth, M. Schroedner, A. Konkin, U. Zhokhavets, G. Gobsch, P. Scharff, and S. Sensfuss, "The influence of the optoelectronic properties of poly(3-alkylthiophenes) on the device parameters in flexible polymer solar cells," *Organic Electronics*, vol. 6, no. 2, pp. 65 – 77, 2005. (Cited on page 31.)

[125] G. Malloci, L. Chiodo, A. Rubio, and A. Mattoni, "Structural and optoelectronic properties of unsaturated ZnO and ZnS nanoclusters," *J. Phys. Chem. C*, vol. 116, pp. 8741–8746, 2012. (Cited on pages 31, 33, and 46.)

[126] J. Mawyin, I. Shupyk, M. Wang, G. Poize, P. Atienzar, T. Ishwara, J. R. Durrant, J. Nelson, D. Kanehira, N. Yoshimoto, C. Martini, E. Shilova, P. Secondo, H. Brisset, F. Fages, and J. Ackermann, "Hybrid heterojunction nanorods for nanoscale controlled morphology in bulk heterojunction solar cells," *J. Phys. Chem. C*, vol. 115, no. 21, pp. 10881–10888, 2011. (Cited on page 31.)

[127] A. Dmytruk, I. Dmitruk, I. Blonskyy, R. Belosludov, and Y. Kawazoe, "ZnO clusters: Laser ablation production and time-of-flight mass spectroscopic study," *Microel. J.*, vol. 40, pp. 218–220, 2009. (Cited on pages 31 and 43.)

[128] C. Caddeo, G. Malloci, G.-M. Rignanese, L. Colombo, and A. Mattoni, "Electronic properties of hybrid zinc oxide-oligothiophenes nanostructures," *J. Phys. Chem. C*, vol. 116, pp. 8174–8180, 2012. (Cited on page 32.)

[129] G. Onida, L. Reining, and A. Rubio, "Electronic excitations: density-functional versus many-body Green's-function approaches," *Rev. Mod. Phys.*, vol. 74, p. 601, 2002. (Cited on page 33.)

[130] D. E. Clemmer, N. F. Dalleska, and P. B. Armentrout, "Reaction of Zn + with NO2. The gas-phase thermochemistry of ZnO," *J. Chem. Phys.*, 1991. (Cited on pages 33 and 34.)

[131] C. A. Fancher, H. L. de Clercq, O. C. Thomas, D. W. Robinson, and K. H. Bowen, "Zinc oxide and its anion: A negative ion photoelectron spectroscopic study," *J. Chem. Phys.*, vol. 109, pp. 8426–8429, 1998. (Cited on pages 33 and 34.)

[132] C. W. Bauschlicher and H. Partridge, "A comparison of ZnO and ZnO^-," *J. Chem. Phys.*, vol. 109, pp. 8430–8434, 1998. (Cited on page 34.)

[133] B. Wang, X. Wang, and J. Zhao, "Atomic Structure of the Magic (ZnO)60 Cluster: First-Principles Prediction of a Sodalite Motif for ZnO Nanoclusters," *J. Phys. Chem. C*, 2010. (Cited on pages 34, 44, 46, and 55.)

[134] B. Wang, S. Nagase, J. Zhao, and G. Wang, "Structural growth sequences and electronic properties of zinc oxide clusters (ZnO)n (n=2-18)," *The Journal of Physical Chemistry C*, vol. 111, no. 13, pp. 4956–4963, 2007. (Cited on page 34.)

[135] C. Li, W. Guo, Y. Kong, , and H. Gao, "First-principles study on ZnO nanoclusters with hexagonal prism structures," *Appl. Phys. Lett.*, vol. 90, p. 223102, 2007. (Cited on page 34.)

[136] B. Meyer and D. Marx, "Density-functional study of the structure and stability of ZnO surfaces," *Phys. rev. B*, vol. 67, p. 035403, 2003. (Cited on page 34.)

[137] T. Jirsak, J. Dvorak, and J. A. Rodriguez, "Chemistry of thiophene on ZnO, S/ZnO, and Cs/ZnO surfaces: Effects of cesium on desulfurization processes," *J. Phys. Chem. B*, vol. 103, no. 26, pp. 5550–5559, 1999. (Cited on page 35.)

[138] G. Mattioli, F. Filippone, P. Giannozzi, R. Caminiti, and A. A. Bonapasta, "Ab initio theoretical investigation of phthalocyanineâsemiconductor hybrid systems," *Chem. Mater.*, vol. 21, no. 19, pp. 4555–4567, 2009. (Cited on page 37.)

[139] Z. Jia, K. Peng, Y. Li, and R. Zhu, "Preparation and photocatalytic performance of porous ZnO microrods loaded with ag," *Transactions of Nonferrous Metals Society of China*, vol. 22, no. 4, pp. 873 – 878, 2012. (Cited on page 43.)

[140] W. Sangthong, J. Limtrakul, F. Illas, and S. T. Bromley, "Predicting transition pressures for obtaining nanoporous semiconductor polymorphs: oxides and chalcogenides of zn, cd and mg," *Phys. Chem. Chem. Phys.*, vol. 12, pp. 8513–8520, 2010.

[141] X. Wang, W. Liu, J. Liu, F. Wang, J. Kong, S. Qiu, C. He, and L. Luan, "Synthesis of nestlike ZnO hierarchically porous structures and analysis of their gas sensing properties," *ACS Applied Materials and Interfaces*, vol. 4, no. 2, pp. 817–825, 2012. (Cited on page 43.)

[142] X. Wang, B. Wang, L. Tang, L. Sai, and J. Zhao, "What is atomic structures of (ZnO)34 magic cluster?," *Phys. Lett. A*, vol. 374, pp. 850–853, 2010. (Cited on page 43.)

[143] M. Zhao, Y. Xia, Z. Tan, X. Liu, and L. Mei, "Design and energetic characterization of ZnO clusters from first-principles calculations," *Phys. Lett. A*, vol. 372, no. 1, pp. 39 – 43, 2007. (Cited on page 43.)

[144] F. De Angelis and L. Armelao, "Optical properties of ZnO nanostructures: a hybrid dft/tddft investigation," *Phys. Chem. Chem. Phys*, vol. 13, pp. 467–475, 2011. (Cited on pages 44, 45, 48, and 74.)

[145] M. A. Zwijnenburg, C. Sousa, F. Illas, and S. T. Bromley, "The fate of optical excitations in small polyhedral zns clusters: A theoretical study of the excitation and localization of electrons in zn4s4 and zn6s6," *J. Chem. Phys.*, vol. 134, p. 064511, 2011. (Cited on page 44.)

[146] M. A. Zwijnenburg, F. Illas, and S. T. Bromley, "The fate of optical excitations in small hydrated zns clusters: a theoretical study into the effect of hydration on the excitation and localisation of electrons in zn4s4 and zn6s6," *Phys. Chem. Chem. Phys.*, vol. 13, pp. 9311–9317, 2011. (Cited on page 44.)

[147] C. Caddeo, G. Malloci, F. De Angelis, L. Colombo, and A. Mattoni, "Optoelectronic properties of $(ZnO)_{60}$ isomers," *Phys. Chem. Chem. Phys.*, vol. 14, pp. 14293–14298, 2012. (Cited on page 44.)

[148] A. A. Al-Sunaidi, A. A. Sokol, C. R. A. Catlow, and S. M. Woodley, "Structures of zinc oxide nanoclusters:

As found by revolutionary algorithm techniques," *J. Phys. Chem. C*, vol. 112, pp. 18860–18875, 2008. (Cited on page 44.)

[149] B. Wang, X. Wang, G. Chen, S. Nagase, and J. Zhao, "Cage and tube structures of medium-sized zinc oxide clusters (ZnO)n (n=24, 28, 36, and 48)," *J. Chem. Phys.*, 2008. (Cited on page 44.)

[150] D. J. Binks and R. W. Grimes, "Incorporation of monovalent ions in ZnO and their influence on varistor degradation," *Journal of the American Ceramic Society*, vol. 76, no. 9, pp. 2370–2372, 1993. (Cited on page 44.)

[151] J. P. Perdew, K. Burke, and M. Ernzerhof, "Generalized gradient approximation made simple," *Phys. Rev. Lett.*, vol. 77, pp. 3865–3868, 1996. (Cited on pages 46 and 74.)

[152] S. Lias, J. Bartmess, J. Liebman, J. Holmes, R. Levin, and W. Mallard, *NIST Chemistry WebBook, NIST Standard Reference Database Number 69, Eds. P.J. Linstrom and W.G. Mallard*. National Institute of Standards and Technology, Gaithersburg MD, 2011. (Cited on page 47.)

[153] J. M. Azpiroz, E. Mosconi, and F. De Angelis, "Modeling ZnS and ZnO nanostructures: Structural, electronic, and optical properties," *J. Phys. Chem. C*, vol. 115, no. 51, pp. 25219–25226, 2011. (Cited on pages 48 and 49.)

[154] M. Feng, J. Zhao, and H. Petek, "Atomlike, hollow-core-bound molecular orbitals of c60," *Science*, vol. 320, no. 5874, pp. 359–362, 2008. (Cited on page 48.)

[155] N. Spallanzani, C. A. Rozzi, D. Varsano, T. Baruah, M. R. Pederson, F. Manghi, and A. Rubio, "Photoexcitation of a light-harvesting supramolecular triad: A time-dependent dft study," *J. Phys. Chem. B*, vol. 113, no. 16, pp. 5345–5349, 2009. (Cited on page 48.)

[156] Z. Zhang, P. Han, X. Liu, J. Zhao, H. Jia, F. Zeng, and B. Xu, "First principle calculations of the electronic properties of the fullerene derivative as an electron acceptor in organic solar cells," *J. Phys. Chem. C*, vol. 112, no. 48, pp. 19158–19161, 2008. (Cited on page 48.)

[157] L. Ley, R. A. Pollak, F. R. McFecly, S. I. Kowalczyk, and D. A. Shirley, "Total valence-band densities of states of

iii-v and ii-vi compounds from x-ray photoemission spectroscopy," *Phys. Rev. B*, vol. 9, pp. 600–621, 1974. (Cited on page 48.)

[158] J. Chen, H. Liu, W. A. Weimer, M. D. Halls, D. H. Waldeck, and G. C. Walker *J. Am. Chem. Soc.*, vol. 124, p. 9035, 2002. (Cited on page 57.)

[159] Y. K. Kang, O.-S. Lee, P. Deria, S. H. Kim, T.-H. Park, D. A. Bonnell, J. G. Saven, and M. K. Therien *Nano Lett.*, vol. 9, pp. 1414–1418, 2009. (Cited on page 57.)

[160] C. Caddeo, C. Melis, L. Colombo, and A. Mattoni, "Understanding the helical wrapping of P3HT on carbon nanotubes," *J. Phys. Chem. C*, vol. 114, pp. 21109–21113, 2010. (Cited on page 58.)

[161] S. N. Wood, "Thin plate regression splines," *J. R. Stat. Soc. Ser. B*, vol. 65, no. 1, pp. 95–114, 2003. (Cited on page 59.)

[162] S. S. Tallury and M. A. Pasquinelli, "Molecular dynamics simulations of polymers with stiff backbones interacting with single-walled carbon nanotubes.," *J. Phys. Chem. B*, vol. 114, pp. 9349–55, 2010. (Cited on page 61.)

[163] I. Gurevitch and S. Srebnik, "Monte carlo simulation of polymer wrapping of nanotubes," *Chem. Phys. Lett.*, vol. 444, pp. 96–100, 2007. (Cited on page 64.)

[164] R. G. S. Goh, N. Motta, J. M. Bell, and E. R. Waclawik, "Effects of substrate curvature on the adsorption of poly(3-hexylthiophene) on single-walled carbon nanotubes," *Appl. Phys. Lett.*, vol. 88, pp. 2–4, 2006. (Cited on page 64.)

[165] B. K. Kuila, S. Malik, S. K. Atabyal, and A. K. Nandi, "In-situ synthesis of soluble poly(3-hexylthiophene)/multiwalled carbon nanotube composite: Morphology, structure, and conductivity," *Macromolecules*, vol. 40, pp. 278–287, 2007. (Cited on page 64.)

[166] S. Daresbury, W. Smith, D. Laboratory, and C. Dean, "DL POLY: A macromolecular simulation package." (Cited on page 71.)

[167] J. Ponder and D. Case *Adv. Prot. Chem.*, vol. 66, pp. 27–85, 2003. (Cited on page 71.)

[168] J. Li, T. Zhu, C. J. Cramer, and D. G. Truhlar *J. Phys. Chem. A*, vol. 102, pp. 1820–1831, 1998. (Cited on page 73.)

[169] R. R. Johnson, C. A. T. Johnson, and M. L. Klein, "The nature of dna-base-carbon-nanotube interactions," *small*, vol. 6, pp. 31–34, 2010. (Cited on page 73.)

[170] "TURBOMOLE V6.2 2010, a development of University of Karlsruhe and Forschungszentrum Karlsruhe GmbH, 1989-2007, TURBOMOLE GmbH, since 2007; available from `http://www.turbomole.com`." (Cited on page 73.)

[171] F. Weigend and R. Ahlrichs, "Balanced basis sets of split valence, triple zeta valence and quadruple zeta valence quality for H to Rn: Design and assessment of accuracy," *Phys. Chem. Chem. Phys. (Inc. Far. Trans.)*, vol. 7, pp. 3297–3305, 2005. (Cited on page 73.)

[172] K. Eichkorn, O. Treutler, H. Ohm, M. Haser, and R. Ahlrichs, "Auxiliary basis sets to approximate coulomb potentials," *Chem. Phys. Lett*, vol. 240, pp. 283–289, 1995. (Cited on page 74.)

[173] M. Sierka, A. Hogekamp, and R. Ahlrichs, "Fast evaluation of the Coulomb potential for electron densities using multipole accelerated resolution of identity approximation," *J. Chem. Phys.*, 2003. (Cited on page 74.)

[174] O. Treutler and R. Ahlrichs, "Efficient molecular numerical integration schemes," *J. Chem. Phys.*, 1995. (Cited on page 74.)

[175] S. F. Boys and F. Bernardi, "The calculation of small molecular interactions by the differences of separated total energies. some procedures with reduced errors," *Mol. Phys.*, vol. 19, pp. 553–566, 1970. (Cited on page 74.)

[176] A. D. Becke *J. Chem. Phys.*, vol. 88, p. 1053, 1988. (Cited on page 74.)

[177] S. J. Vosko, L. Wilk, and M. Nusair *Can. J. Phys.*, vol. 58, p. 1200, 1980.

[178] J. P. Perdew *Phys. Rev. B*, vol. 33, pp. 8822–8824, 1986. (Cited on page 74.)

[179] A. D. Becke, "Density-functional thermochemistry. iii. the role of exact exchange," *J. Chem. Phys*, vol. 98, p. 5648, 1993. (Cited on page 74.)

[180] M. Cossi, N. Rega, G. Scalmani, and V. Barone, "Energies, structures, and electronic properties of molecules in solution with the c-pcm solvation model," *J. Comput. Chem.*, vol. 24, no. 6, pp. 669–681, 2003. (Cited on page 74.)

[181] M. Cossi and V. Barone, "Time-dependent density functional theory for molecules in liquid solutions," *J. Chem. Phys.*, vol. 115, no. 10, pp. 4708–4717, 2001. (Cited on page 74.)

[182] M. J. F. et al., "Gaussian 09, Revision A.02." Gaussian, Inc., Wallingford, CT, 2003. (Cited on page 74.)

COLOPHON

This document was typeset using the typographical look-and-feel `classicthesis` developed by André Miede. The style was inspired by Robert Bringhurst's seminal book on typography "*The Elements of Typographic Style*". `classicthesis` is available for both LaTeX and LyX:

http://code.google.com/p/classicthesis/

Final Version as of May 13, 2013 (`classicthesis`).